

1 Responses of estuarine circulation to the morphological evolution in a
2 convergent, microtidal estuary

3 Rui Zhang^a, Bo Hong^b, Lei Zhu^{a,c,d}, Wenping Gong^{a,c*}, Heng Zhang^{a,c,d}

4 a- School of Marine Sciences, SunYat-sen University, Guangzhou, China, 510275

5 b- School of Civil Engineering and Transportation, South China University of
6 Technology, Wushan RD., Tianhe District, Guangzhou 510641, China

7 c- Southern Marine Science and Engineering Guangdong Laboratory (Zhuhai), Zhuhai
8 519000, China

9 d- Pearl River Estuary Marine Ecosystem Research Station, Ministry of Education,
10 Zhuhai, 519082, China

11
12 **Abstract:**

13 The Huangmaohai Estuary (HE) is a funnel-shaped microtidal estuary in the west
14 of the Pearl River Delta (PRD) in southern China. Since China's reform and opening up
15 in 1978, extensive human activities have occurred and greatly changed the estuary's
16 topography, and modified its hydrodynamics. In this study, we examined the
17 morphological evolution by analyzing remote sensing data with ArcGIS tools and
18 studied the responses of hydrodynamics to the changes in topography from 1977 to
19 2010 by using the Delft3d model. We took the changes in estuarine circulation during
20 neap tides in dry seasons as an example. The results show that human reclamation
21 caused a narrowing of the estuary, and channel dredging deepened the estuary. These
22 human activities changed both the longitudinal and lateral estuarine circulations. The
23 longitudinal circulation was observed to increase with the deepening and narrowing of
24 the estuary. The lateral circulation experienced changes in both the magnitude and
25 pattern. The momentum balance analysis shows that when the depth and width changed
26 simultaneously, the longitudinal estuarine circulation was modulated by both the

* Supported by the National Natural Science Foundation of China under contract Nos 51761135021,
41506102 and 41890851.

** Corresponding author, E-mail: gongwp@mail.sysu.edu.cn

27 channel deepening and width reduction, in which the friction, pressure gradient force,
28 and advection terms were altered. The analysis of the longitudinal vortex dynamics
29 indicates that the changes in the vertical shear of the longitudinal flow, lateral salinity
30 gradient, and vertical mixing were responsible for the change in the lateral circulation.
31 The changes in water depth are the dominant factor affecting lateral circulation intensity.
32 This study has implications for sediment transport and morphological evolution in
33 estuaries heavily impacted by human interventions.

34

35 **Keywords:** Estuarine circulation, Morphological evolution, Huangmaohai Estuary

36

37 **1. Introduction**

38

39 Estuarine circulation, the tidally averaged flow in estuaries including both the
40 longitudinal and lateral circulations, is the main driving force for the transport of
41 sediment, pollutants, and other materials, and also one of the primary factors affecting
42 the ecological environment of estuaries (Kjerfve et al., 1981). Estuarine circulation is
43 influenced by many factors (Geyer and Maccready, 2014), such as sea-level
44 fluctuations (Wilson and Filadelfo, 1986), river discharge, tides (Pritchard, 1952), and
45 winds (Scully et al., 2005; Waterhouse et al., 2013; Geyer and Maccready, 2014; Salles
46 et al., 2015; Chen et al., 2020a). Topography in an estuary has a significant effect on
47 the pattern and intensity of the estuarine circulation (Fischer, 1976; Dyer, 1977).
48 Human activities may change the estuarine topography, leading to changes in the
49 estuarine circulation and associated material transport. Therefore, a study of the
50 estuarine circulation and its response to human activities is essential for integrated
51 management of the development of estuarine resources, and the maintenance of the
52 estuary's ecological health.

53 Channel deepening by dredging and sand mining is a common practice in the
54 development and maintenance of navigable channels in estuaries. Generally speaking,
55 channel deepening can increase the longitudinal estuarine circulation by decreasing the

56 bottom friction and increasing the baroclinic forcing which is proportional to the water
57 depth (Amin, 1983; Chernetsky et al., 2010; Winterwerp, 2011). On the other hand, the
58 increase in water depth can also increase the salt intrusion and decrease the along-
59 channel density gradient, thus reducing the baroclinic forcing. Channel deepening also
60 affects the estuarine circulation in other ways, such as increasing the Stokes transport
61 and the associated compensating return flow (Amin, 1983), altering the nonlinear tidal
62 rectification (Li and O'Donnell, 1997), and tidal asymmetry in mixing between flood
63 and ebb tides (tidal straining) (Simpson, 1990). Therefore, the effect of channel
64 deepening is an intricate balance between these reinforcing and/or competing effects.
65 Chant et al. (2018) demonstrated that a relatively small (15%) increase in water depth
66 can result in a double exchange flow. They attributed this increase to the increase in
67 along-channel salinity gradient and/or a reduction in vertical mixing, but they did not
68 give a clear distinction about how these two effects work together and which is
69 dominant.

70 Change in estuary width is another aspect of topographic change in estuaries and
71 is mainly caused by reclamation and utilization of salt marshes, construction of coastal
72 protection structures along the estuarine banks. Change in estuary width generates a
73 change in the estuarine convergence, and therefore a change in the estuarine circulation.
74 Burchard et al. (2014) concluded that an increase in the estuarine convergence results
75 in an enhancement or reduction of the longitudinal estuarine circulation as increased
76 estuarine convergence can reduce or even reverse the straining-induced circulation,
77 though the advection-induced circulation is increased. Changes in estuarine width can
78 also modify the lateral circulation and feedback to the generation of the longitudinal
79 estuarine circulation through the change in lateral advection (Lacy et al., 2003; Lerczak
80 and Rockwell Geyer, 2004; Scully et al., 2009; Burchard et al., 2010; Burchard et al.,
81 2014). Lerczak and Rockwell Geyer (2004) suggested that lateral effects on the
82 longitudinal estuarine circulation would be stronger in narrower estuaries given a
83 constant lateral salinity gradient. Schulz et al. (2015) investigated the impact of the
84 depth-to-width ratio of the estuarine cross-section on the longitudinal estuarine

85 circulation and found that the longitudinal estuarine circulation exhibits a distinct
86 maximum in medium-wide channels. They diagnosed the mechanisms for such a
87 phenomenon and attributed it to the sensitivities of the straining- and advection-induced
88 circulations on the changes in depth-to-width ratio.

89 As revealed by Lerczak and Geyer (2004) and other researchers (Chen et al.,
90 2020b), lateral processes play important roles in the generation of the longitudinal
91 estuarine circulation. In estuaries, the pattern and intensity of lateral circulation are
92 controlled by three processes (Li et al., 2014): vertical shear of the longitudinal current
93 affecting the tilting of planetary vorticity, lateral salinity gradient (baroclinicity), and
94 diffusion. The longitudinal estuarine circulation can affect the lateral circulation
95 through all the mentioned three factors. Therefore, the interaction between the
96 longitudinal and lateral processes is fully nonlinear and quite complex. Though these
97 interactions have been discussed in detail (Scully et al., 2009; Li et al., 2017), several
98 questions remain open: How does the longitudinal estuarine circulation affect the
99 intensity and vortex structure of the lateral circulation? Does a decreased/increased
100 lateral circulation necessarily lead to a weakened/strengthened longitudinal circulation?
101 These questions become complicated in an estuary where both width and depth vary.
102 Previous studies showed that the narrowing and deepening of the Yangtze River
103 Estuary resulted in an enhanced longitudinal estuarine circulation (Zhu, 2018), which
104 changed from transversely sheared to vertically sheared. The estuarine stratification
105 was also found to be strengthened, along with an increase in the intensity of lateral
106 circulation. Zhu et al. (2015) investigated the influences of channel deepening and
107 widening on the tidal and nontidal circulations of Tampa Bay, USA, and found that the
108 nontidal circulation was strengthened by these human interventions. However, how
109 does the estuarine circulation respond to both narrowing and deepening/shallowing of
110 the estuary? What happens when the narrowing rate is much larger or smaller than the
111 deepening rate in an estuary? Here the narrowing rate is the ratio of the difference of
112 cross-section widths between two consecutive years divided by the width in the earlier

113 year. Similarly, the deepening rate is the ratio of the difference of water depth in the
114 cross-section between the two consecutive years divided by the earlier year's depth.

115 Here we try to address the above questions by studying the changes in the estuarine
116 circulation from 1977 to 2010 in the Huangmaohai Estuary (HE), a microtidal estuary
117 in the southwest of the Pearl River Delta (PRD), which experienced different stages of
118 topographic changes under human activities: narrowing and deepening (1977-1994, and
119 2003-2010), and narrowing and shallowing (1994-2003). Thus, it provided a good
120 opportunity to study the effect of human activities induced morphological evolution on
121 the estuarine circulation.

122 In this study, we used a state-of-the-art three-dimensional baroclinic model (Delft
123 3d) to simulate the changes in hydrodynamics in the HE in different years and examined
124 the changes in intensities of the longitudinal and lateral estuarine circulations, followed
125 by an analysis of the mechanisms for these changes by conducting diagnostic analyses
126 of the momentum balance. The structure of the rest of the paper is as follows. Section
127 2 introduces the study area and numeral model. Section 3 presents the results of
128 morphological evolution and changes in the estuarine circulation. Then, the
129 mechanisms for the changes in estuarine circulation are investigated using the
130 momentum and vortex balance equations in Section 4. Finally, the conclusions are
131 presented in Section 5.

132

133 **2. Study area and methodology**

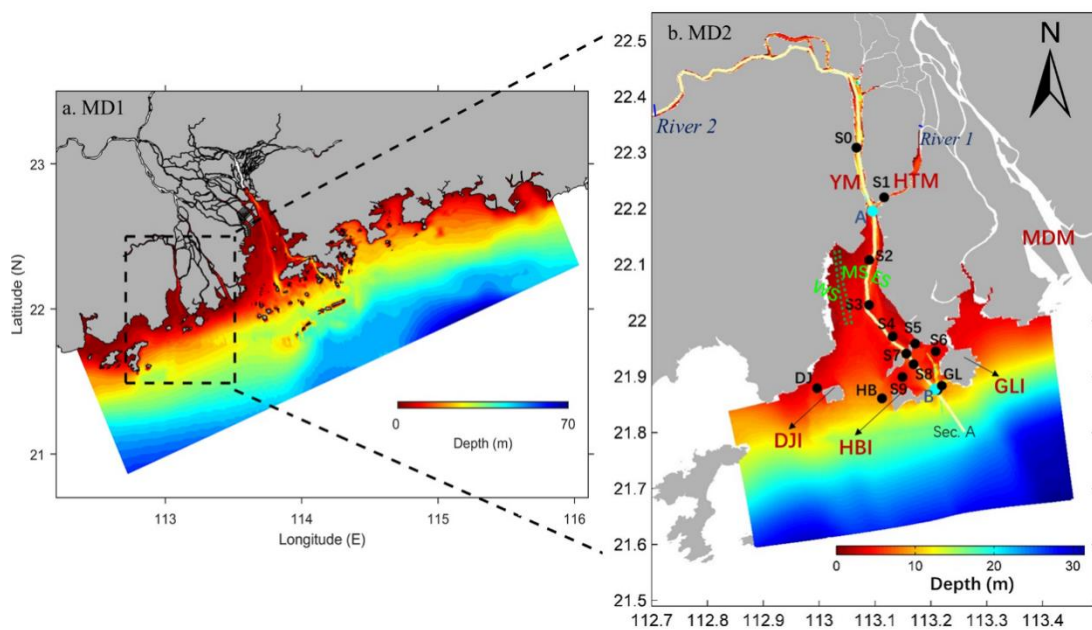
134

135 **2.1 Study area**

136

137 The HE is located in the west of the PRD in southern China and exhibits a
138 distinctly convergent geometry, with a latitude ranging from 21°50' to 22°13' N and
139 a longitude ranging from 113°00' to 113°51' E (Fig. 1). The estuary is composed of a
140 bay (Huangmao Bay) and a tidal river. The bay is trumpet-shaped with an area of 409

141 km². It has a complex bathymetry comprising of two channels and three shoals, namely
 142 the West Channel and East Channel, the West Shoal, Middle Shoal, and East Shoal. In
 143 recent decades, the West Channel is observed to shrink and almost disappear now (Jia
 144 et al., 2012). The width of the bay is 30 km at the estuary mouth and decreases to 1.8
 145 km at the head. The mean water depth of the bay is 4.5 m (Gong et al., 2014). The bay
 146 is connected to the upstream river catchment by two constrictions (Yamen and
 147 Hutiaomen Outlets). Several islands, namely Dajin Island, Hebao Island, and Gaolan
 148 Island, are scattered at the estuary's mouth (shown in Fig. 1b).



149
 150 Fig. 1. The study area (Huangmaohai estuary) and observation stations. Major topographic
 151 features and domains of the nested modeling system over (a) the PRD and (b) the HE and its
 152 adjacent waters. YM = Yamen; HTM = Hutiaomen; MDM = Modaomen; DJI = Dajing Island;
 153 GLI = Gaolan Island; HBI = Hebao Island. The black dots (S0–S9, DJ, HB, and GL) in the
 154 MD2 domain are stations of field deployments in March 2010. The solid lines represent the
 155 along-channel transect (Section A (AB)), which lies in the East Channel. The green dotted lines
 156 represent the West Channel in 1977. Three shoals are shown in (b): West Shoal (WS), Middle
 157 Shoal (MS), and East Shoal (ES).

158
 159 The HE has a subtropical monsoon climate, with the precipitation in the wet season
 160 (from May to September) being high. Approximately 80% of the river discharge occurs
 161 during the wet season, with an average discharge of 200.23 m³/s. The tides in the HE
 162 are mixed semidiurnal with dominant semi-diurnal constituents and smaller diurnal

163 constituents. The tidal range is approximately 1.5 m at the mouth and experiences an
164 initial increase from the mouth towards the head owing to a strong convergence of the
165 bay width. Further landward in the tidal river beyond the bay head, the tidal range
166 decreases by the overwhelming bottom friction (Gong et al., 2012). The tidal current
167 velocity ranges from 0.5 m/s to 1.5 m/s (Huang, 2011), and is higher in deep channels
168 than on shallow shoals. The tidal currents are generally rectilinear in deep channels but
169 become more rotary in shallow shoals.

170 Since the 1980s, human activities have been intense in the HE. A hydroelectric
171 power project upstream of the estuary, channel dredging, sand mining, and construction
172 of Gaolan Island levees have led to great changes in the HE's topography. Also, the HE
173 has rich tidal flat resources and endured frequent reclamation activities. From 1965 to
174 2003, a total of 142.29 km² tidal flat was reclaimed, with an average reclamation rate
175 of 3.74 km²/a, and the reclamation rate continuously but gradually increased during that
176 period. After 2003, the reclamation rate slowed down. In terms of channel dredging,
177 the Yamen Waterway Project was conducted in 1997 to deepen the channel between
178 S0 and S3 in Fig. 1b (Luo, 2010). In April 2005, the Yamen Channel regulation project
179 was implemented to alleviate the serious siltation in the channel, with the channel being
180 dredged to a depth of about 6 m.

181 In the following, we chose 1977, 1994, 2003, and 2010 as the representative years
182 to study the typical scenarios of bathymetric changes in the HE.

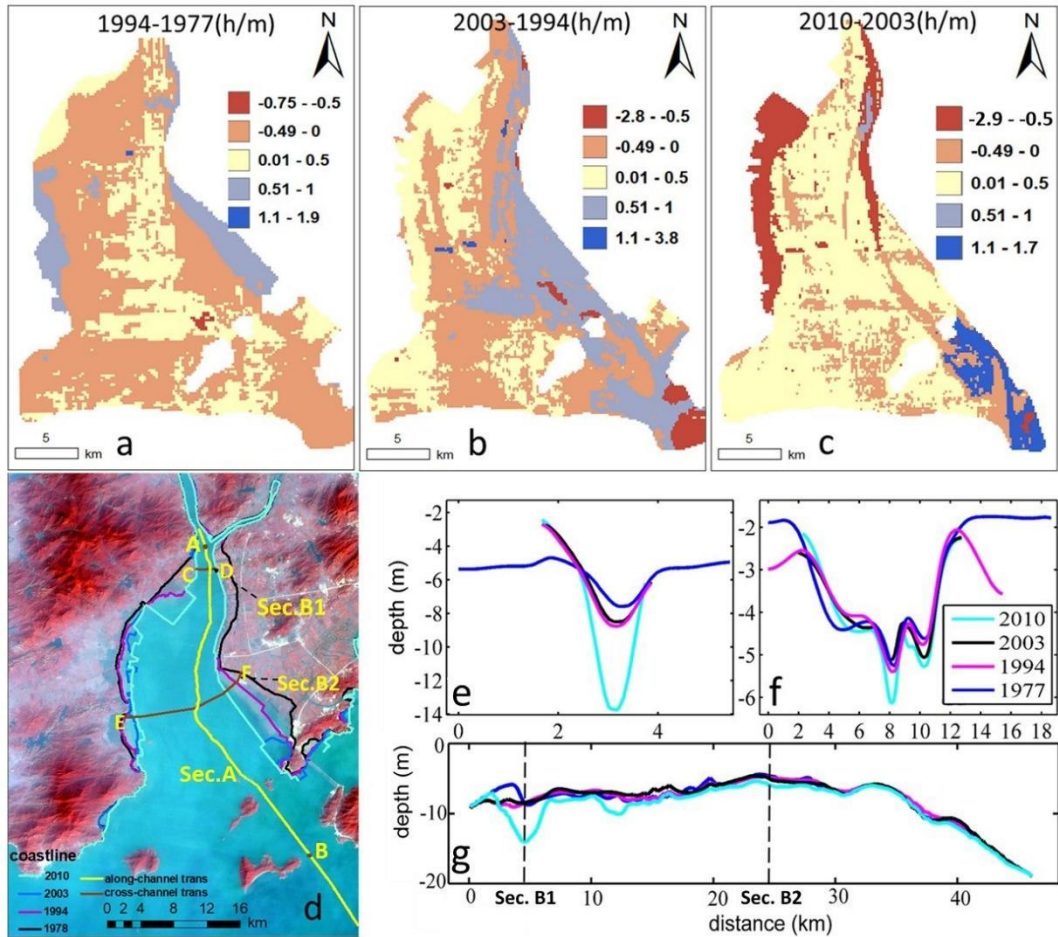
183

184 **2.2 Remote sensing and topographic data**

185

186 Remote sensing data were used for coastline extraction and included Landsat
187 Multi-Spectral Scanner (MSS) data, Landsat Thematic Mapper (TM) data, and Landsat
188 Operational Land Imager (OLI) data. A total of 66 images (Table 1) were downloaded
189 from <http://www.gscloud.cn/>. These data were firstly processed by geometric (with
190 errors less than 0.5 pixels (Ai et al., 2019)) and atmospheric corrections by the ENVI
191 5.3 software. The topography data inside the HE were derived from nautical charts

192 (1977, 1994, 2003, and 2010), published by the Navigation Safety Guarantee Bureau.
 193 The filling and excavation toolbox of ArcGIS was used to calculate the difference
 194 between the volumes in two consecutive periods by superimposing the corresponding
 195 Digital Elevation Models (DEM). We thus obtained the average siltation rates of the
 196 study area over different years (Figs. 2a-c).



197
 198 Fig. 2. (a-c) Water depth difference between years ((a)1994-1977; (b)2003-1994; (c)2010-
 199 2003), where the positive value indicates “deepening” and the negative one indicates “siltation”,
 200 (d) Shorelines of 1977-2010 and locations of two cross-sections (AB: Sec. A; CD: Sec. B1;
 201 Sec. B2); (e, f, and g) The bathymetric evolutions at Sections B1, B2, and A in 1977, 1994,
 202 2003, and 2010.

203
 204

Table 1. Data of remote sensing images

Time	Satellite	Image sensor	Resolution/m	Path/Row	Memory space
1973,1978	Landsat3	MSS	78	122/45	142G
1986-2011	Landsat5	TM	30		

2012	Landsat7	ETM	30
2013-2018	Landsat8	OLR	30

205

206 **2.3 Numerical model setting up and validation**

207

208 The numerical model Delft3d, a fully three-dimensional hydrodynamic water quality
 209 model (Lesser et al., 2004), was used to simulate the hydrodynamics in the HE. Its
 210 algorithm can guarantee the conservation of mass, momentum, and energy. The model
 211 grid consisted of a nesting grid system, with the MD1 (parent model, Fig. 1a) covering
 212 the whole PRD, and the MD2 (child model) covering the HE. For the MD2 model, a
 213 curvilinear orthogonal grid of 269*620 was established, with the horizontal resolution
 214 ranging from 64 m in the channel to 324 m at the ocean boundary. Vertically, the grid
 215 was discretized into 10 layers of σ coordinate. The model system used here is the same
 216 as the one in Chen et al. (2020a). The MD1, based on a 1-D (for the river network) and
 217 3-D coupled model, covered the whole PRD and the coastal region with a horizontal
 218 resolution of 2 km near the open boundary and 500 m inside the PRE (Fig. 1a). The
 219 Open sea boundaries for the MD1 comprised hourly tidal elevations and depth-averaged
 220 tidal currents derived from nine tidal constituents (M2, S2, N2, K2, K1, O1, P1, Q1,
 221 and M4) taken from the global tidal circulation model (TPXO 8,
 222 http://volkov.oce.orst.edu/tides/tpxo8_atlas.html) with a resolution of $1/30^\circ$ and daily
 223 water elevation, 3-D temperature, salinity (a constant salinity of 34 psu at the open
 224 ocean boundary) and velocity data from the Hybrid Coordinate Ocean Model
 225 (<https://hycom.org>) with a resolution of $1/12^\circ$ (Chen et al., 2020a). Thus the sources of
 226 water level variation and currents at the offshore boundary in MD1 are: 1) tides; 2) non-
 227 tidal components by external forcings, such as winds, air pressure, water temperature,
 228 and large-scale circulation in the South China Sea. The results from the MD1 were
 229 interpolated to provide ocean boundary conditions for the MD2 model, there were no
 230 “wind and wave effects” in the MD2.

231 As mentioned above, the hydrodynamics in the HE experiences distinct seasonal
 232 variation. The estuarine circulation during the wet season has been extensively studied
 233 before (Chen et al., 2020a; Chen et al., 2020b). Here we choose the dry season to
 234 investigate the changes in the estuarine circulation caused by topographic changes in
 235 different years. We conducted a series of numerical experiments using the bathymetry
 236 data in 1977, 1994, 2003, and 2010. The simulation time was chosen to be from 00:00
 237 on March 1 to 23:00 on March 31 in the dry season, when observation data were
 238 available in 2010. Field measurements were carried out at 14 mooring stations on
 239 March 17th 17:00 to 18th 22:00, 2010. The measured variables included vertical
 240 profiles of current, temperature, and salinity. In all the four scenarios, two upstream
 241 boundaries were specified (Fig. 1b): at River 2 by specifying real-time water level data
 242 from the MD1 model from 00:00 on March 1, 2010, to 23:00 on March 31, 2010, with
 243 a time interval of 1 hour; At River 1 by specifying a constant river discharge of 100
 244 m³/s. The choice of this constant value was based on previous simulation experiences
 245 (Chen et al., 2020a; Chen et al., 2020b). The salinities at the river inflow boundaries
 246 were set to be 0 psu. The only changing condition of the four scenarios was the
 247 topography (Table 2), so the effect of topographic change can be distinguished. The
 248 measured data from 14 stations in 2010 were used to validate the model.

249

250 Table 2. Coastline, bathymetry, salinity, flow, and tidal boundary in the four model scenarios.

Scenario	Coastline	Bathymetrie s	The salinity of the open sea	Flow	Tidal boundary
1977/03	1977	1977	2010/03	2010/03	2010/03
1994/03	1994	1994	2010/03	2010/03	2010/03
2003/03	2003	2003	2010/03	2010/03	2010/03
2010/03	2010	2010	2010/03	2010/03	2010/03

251

252 In this study, the Willmott skill score (SK) was used to evaluate whether the model
 253 result is consistent with the observed data (Willmott, 1981). The SK is defined as:

254
$$SK = 1 - \frac{\sum_{i=1}^n (O_i - M_i)^2}{\sum_{i=1}^n [|M_i - \bar{O}| + |O_i - \bar{O}|]^2} , \quad (1)$$

255 where n is the number of the observed data, M and O are model simulation results
 256 and observations, respectively, and \bar{o} is the average value of the observation data. SK
 257 is used to measure the consistency between the model results and the observations, with
 258 a value between 0 and 1. The larger the value is, the more consistent the simulation
 259 results are with the observed data.

260 Firstly, the water level of the MD2 model was validated. The SKs of the four
 261 observed stations are all above 0.86, indicating that the water level simulation is
 262 reasonable. Secondly, the modeled current directions showed good performance except
 263 for the surface layer at Stations DJ and S0, almost all the SKs are greater than 0.7 (Table
 264 3). The simulation of the current speed is worse than that of the current direction, but
 265 the SKs at most stations are above 0.6, showing a good performance. Lastly, the trends
 266 of observed and simulated salinities are consistent, and almost all the SKs of salinity
 267 validation are above 0.5, especially in S1-S3, showing a good performance of the
 268 salinity simulation.

269 Table 3. Skill scores by comparison of modeled results with observations.

Stations	Current direction			Current speed			Salinity		
	Sur	Mid	Bot	Sur	Mid	Bot	Sur	Mid	Bot
S0	0.18	0.96	0.96	0.77	0.88	0.86	0.32	0.35	0.35
S1	0.94	0.99	0.99	0.65	0.66	0.61	0.94	0.94	0.90
S2	0.78	0.79	0.71	0.83	0.84	0.84	0.84	0.85	0.85
S3	0.87	0.98	0.95	0.34	0.38	0.39	0.92	0.79	0.77
S4	0.84	0.94	0.94	0.53	0.55	0.53	0.77	0.64	0.54
S5	0.86	0.92	0.93	0.66	0.71	0.72	0.37	0.25	0.26
S6	0.79	0.90	0.88	0.68	0.75	0.74	0.15	0.20	0.25
S7	0.82	0.85	0.96	0.74	0.79	0.83	0.86	0.66	0.56
S8	0.84	0.89	0.89	0.59	0.62	0.66	0.82	0.77	0.72
S9	0.80	0.74	0.77	0.54	0.46	0.41	0.59	0.50	0.52
DJ	0.61	0.77	0.77	0.38	0.47	0.51	0.66	0.47	0.37
GL	0.89	0.91	0.93	0.50	0.51	0.49	0.37	0.43	0.41
HB	0.71	0.89	0.89	0.60	0.56	0.56	0.57	0.54	0.53

270
 271 As a whole, the simulation of surface currents is worse than that in other layers,
 272 since winds and waves were not included in our MD2 model simulations, in which the
 273 surface flow is more susceptible to these forcings. The specified river flow at River 2

274 was constant, which may deviate from the real-time data (not available), leading to a
275 poor salinity reproduction at upstream stations. In short, the water level and current are
276 well-validated. The simulation of salinity is generally good, except for some deviations
277 at upstream stations. It shows that the model can reasonably simulate the hydrodynamic
278 processes in the area, and can be used for the following hydrodynamics study in the HE.

279

280 **3. Results**

281

282 **3.1 Morphological evolution**

283

284 Morphological changes between 1977, 1994, 2003, and 2010 are shown in Figs.
285 2a-c. Figure 2a shows that most areas in the HE experienced siltation from 1977 to
286 1994, but the East Channel was deepened by about 0-0.5 m. In the middle of the bay,
287 the nearshore areas were under erosion, and the erosion thickness at the eastern shore
288 was twice that at the western shore. In other areas, the siltation thickness was between
289 0 and 0.5 m. From 1994 to 2003, erosion occurred in the West Shoal, East Channel,
290 East Shoal, and Middle Shoal. Siltation of 0.01-0.5 m happened in the rest of the area,
291 which accounted for most of the HE, so the HE became shallower in 2003. In 2003,
292 siltation in the East Channel was serious and the water depth there became only 2m (Li,
293 2019). From 2003 to 2010, the West Shoal became significantly shallower with a
294 siltation thickness of about 0.5-1m. The East Shoal almost disappeared, and its relict
295 area endured siltation of 1.1-1.7 m, which was mainly due to the construction of coastal
296 protection works. Strong erosion occurred in other areas, especially in the upper bay
297 with a deepening of more than 4m, and the overall water depth of the HE became greater
298 in 2010.

299 Overall, the water depth of the HE changed considerably from 1977 to 2010. It
300 first experienced erosion, then underwent siltation, and followed by erosion again.

301 Figure 2d shows the changes of coastlines for the four representative years. To
302 calculate the rate of geometry convergence, the DSAS tool (Version 5.0) in Arcmap
303 10.3 was used to calculate the end-point rates for cross-shore transects. A more detailed
304 procedure is in Zhang et al. (2019). We chose one longitudinal section along the channel
305 in the estuary and two cross-sections (in Fig. 2d) along the channel for analysis. The
306 longitudinal section (Sec. A) extends from the bay head (point A in Fig. 1b) to the
307 estuary mouth (point B in Fig. 1b), spanning a distance of 50 km. Sec. B1 is located at
308 about 4 km downstream from the bayhead, where the water depth changes sharply in
309 the lateral (or longitudinal) direction (see Fig. 2e). Sec. B2 is approximately 24km
310 downstream from the bayhead and near the null point in the middle of the estuary (see
311 Fig. 2f), and the width of the estuary varied dramatically here (see Fig. 2e). At Sec. A,
312 the water depth near the point of Sec. B1 endured a great change in 2010 due to channel
313 dredging (Fig. 2g). In other periods, the water depth along its course endured gradual
314 deepening. At Sec. B1, the bathymetric change is featured by an increase in water depth
315 and negligible change in width over time. At Sec. B2, both the water depth and width
316 experienced changes from 1977 to 2010, with the depth increased and width decreased
317 (Fig. 2f). The above three sections clearly depict the topographic changes of the estuary
318 in different years.

319

320 **3.2 Changes in the vertically averaged flow and salinity**

321

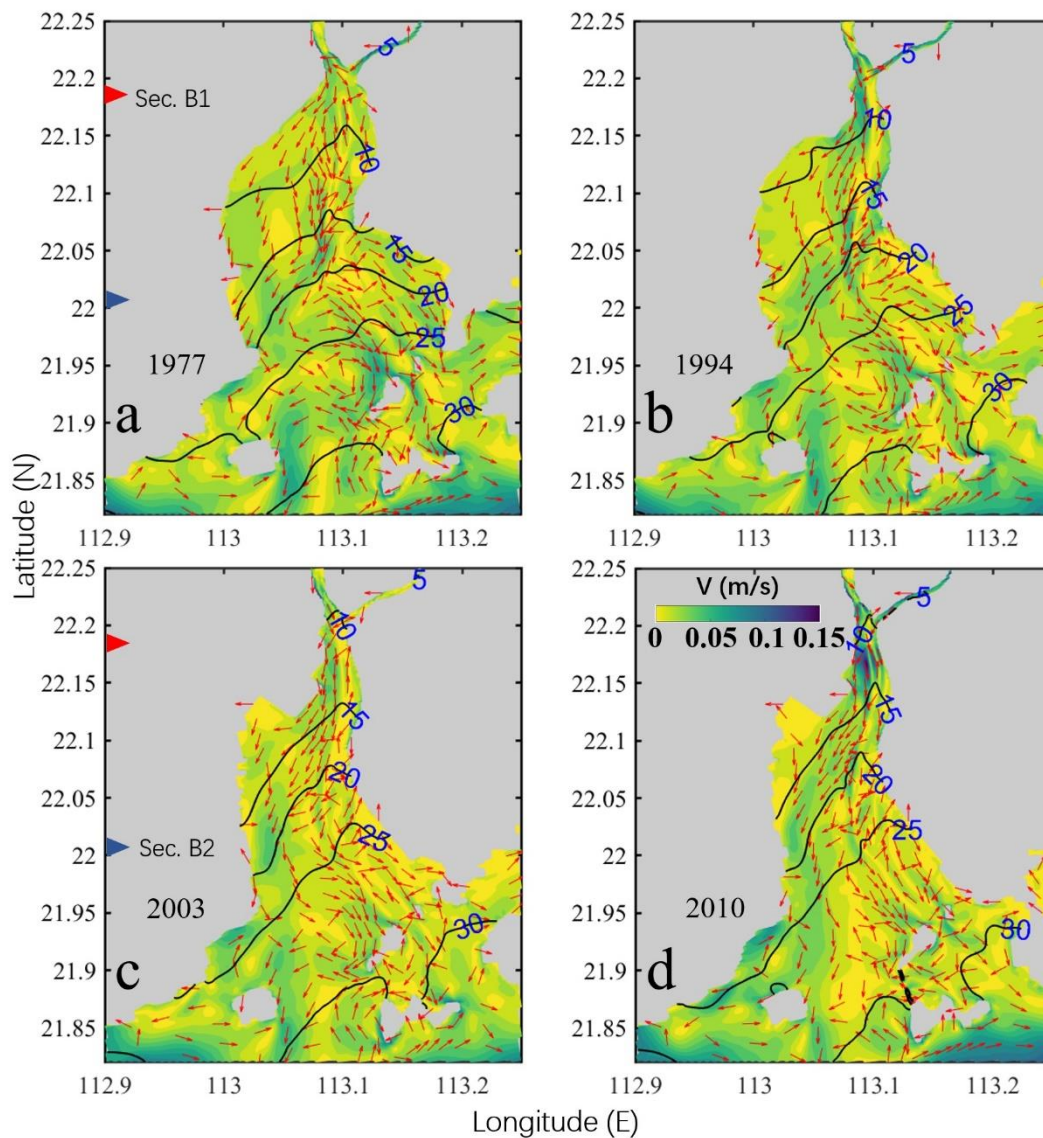
322 Here we present the changes in the tidally and vertically averaged flow and salinity
323 during neap tides in Fig. 3. In 1977 (Fig. 3a), the current speed was generally small,
324 except at the inter-island sections and in the channel. The vertically averaged flow was
325 seaward in the upper bay and the right part of the lower bay (looking landward). It
326 became landward at the left part of the lower bay. In 1994 (Fig. 3b), the current speed
327 was increased in the channel, particularly near Sec.B1. The overall flow pattern was
328 almost similar to that in 1977. In 2003 (Fig. 3c), the flow pattern still kept unchanged
329 when compared to that in previous years. The current speed was decreased relative to

330 that in 1994. In 2010 (Fig. 3d), the seaward flow became more dominant in the upper
331 bay, and more biased southwestward. The seaward flow in the channel was greater than
332 in 2003. The 10 psu isohaline kept moving upstream over time, and reached beyond the
333 bayhead and entered into the tidal river of the estuary in 2010.

334 Overall, we observed that the tidally and vertically averaged flow during neap tides
335 experienced an increase-decrease-increase by the topographic changes, whereas the
336 saltwater consistently intruded more landward.

337 As a supplement, we present the horizontal distributions of tidally averaged
338 surface and bottom circulation and salinity during neap tides for different years in the
339 appendix (Figs. A. 1 and 2). Over the study period, the enhancement of salt intrusion
340 was stronger for the bottom layer and weaker for the surface layer, whereas the increase
341 in residual flow was stronger in the surface layer and weaker in the bottom layer.

342 For the hydrodynamic characteristics of the HE during the flood and ebb tides,
343 Chen et al., (2020a) have investigated the intratidal dynamic processes in detail.



344

345 Fig. 3. Patterns of the tidally and vertically averaged circulation during neap tide (from March
 346 10th 00:00 to 11th 00:00 (25h)) in 1977(a1), 1994(a2), 2003(a3), and 2004(a4). The magnitude
 347 of the current is represented by the color shading, while the current direction is shown by the
 348 arrows. The salinity is depicted by the contour lines. The red and blue triangles depict the
 349 positions of two cross-sections (Sec.B1 and Sec.B2).

350

351 3.3 Changes in the estuarine circulation

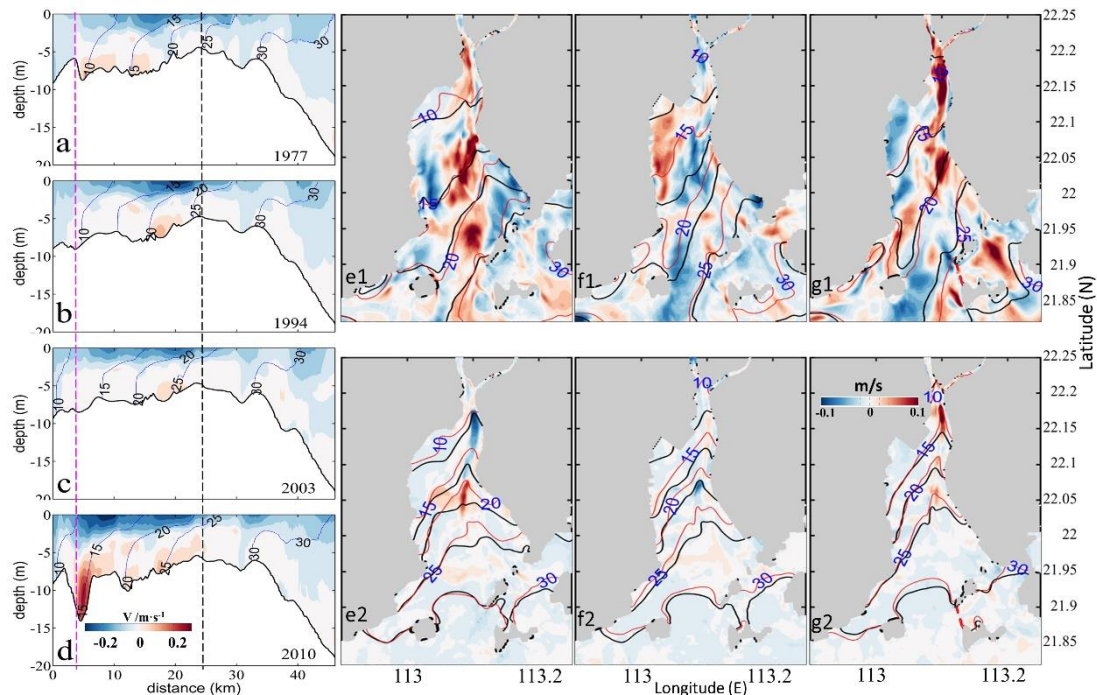
352

353 Figures 4 a-d show that the upper part of the estuary (upstream of the null point)
 354 was highly stratified, and the lower part of the estuary (downstream of the null point)
 355 was well mixed. The classical exchange flow structure was more distinct upstream of

356 the null point. Over time, the surface seaward flow became stronger and more
357 concentrated with the narrowing of the estuary, particularly in 2010. It extended more
358 downstream to near the estuary mouth with the narrowing of the estuary, as evidenced
359 by the extent of the seaward flow of 0.2 m/s. Concomitantly, the bottom landward flow
360 was strengthened and concentrated with the increase in depth. It should be noted that
361 the greatly enhanced estuarine circulation between 3 to 8 km in 2010 (Fig. 4d) could be
362 induced by the intratidal fluctuation of the halocline in response to the large topography
363 change there (Geyer and Nepf, 1996; Chen et al., 2012; Wang et al., 2015).

364 We also present the changes in the surface and bottom current horizontally. Figs.
365 4e1-g1 show that when the estuary deepened (1977-1994 and 2003-2010), the surface
366 current velocity increased in the channel, and when the estuary shoaled (1994-2003),
367 the surface current velocity in the channel decreased. The changes in the bottom current
368 showed a similar trend (Figs. 4e2-g2), except at the upper part of the channel from 1977
369 to 1994, in which the width was considerably decreased.

370 Along with the change in the longitudinal estuarine circulation, the salt intrusion
371 at Sec. A did not change significantly from 1977 to 1994, but increased from 2003 on,
372 particularly in 2010, when the isohaline of 15 psu reached Sec.B1, whose salinities
373 were less than 12 psu in previous years (Figs. 4a-d). The salt intrusions at the surface
374 and bottom gradually increased with the estuary narrowing (Figs. 4e1-g2).



375

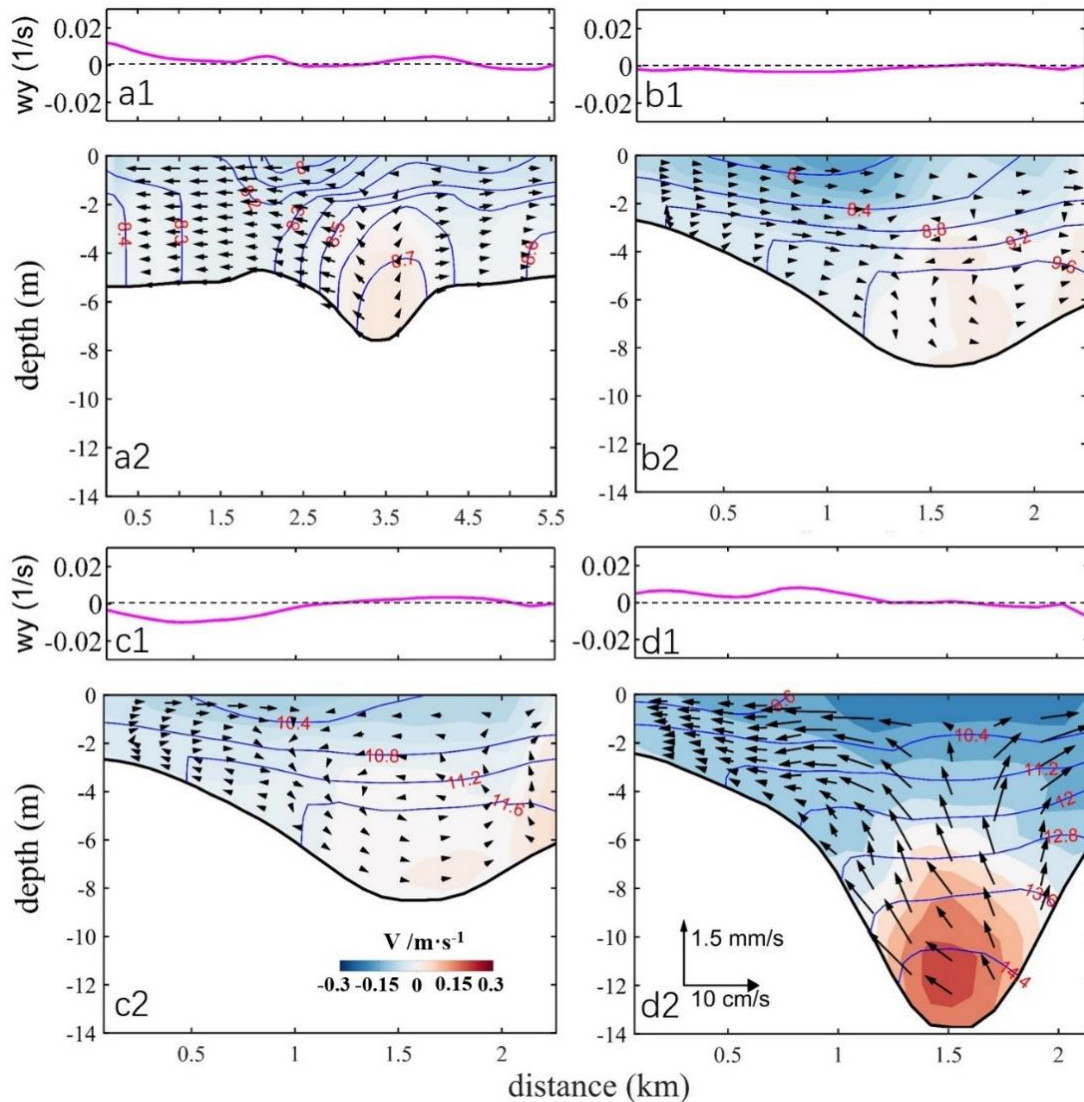
376 Fig. 4. The patterns of the tidally-averaged estuarine circulation during the neap tide (from
 377 March 10th 00:00 to 11th 00:00 (25h)) in March 1977(a), 1994(b), 2003(c), and 2010(d). The
 378 thin lines are the isolines of salinity in a-d. The pink and black dotted lines represent the
 379 locations of Secs. B1 and B2, respectively. The starting point of the X-axis is Point A in Fig.
 380 1b. Surface tidally-averaged current differences from 1977 to 1994(e1), from 1994 to 2003(f1),
 381 and from 2003 to 2010(g1); Bottom tidally-averaged current differences from 1977 to 1994(e2),
 382 from 1994 to 2003(f2), and from 2003 to 2010(g2). The red and black lines represent the
 383 isolines of salinity in the later year and the earlier year.

384

385 To analyze the changes of lateral circulation in the estuary, we show the structure
 386 and intensity of the lateral circulation at the two cross-sections (Figs. 5 and 6).

387 At Sec. B1 (Fig. 5), with the increase of water depth, the salinity difference
 388 between the surface and bottom increased, along with an increase in the bottom salinity.
 389 For the lateral circulation, there was no distinct gyre structure in 1977. In 1994, the
 390 lateral flow was dominated by an eastward flow. In 2003, a clockwise vortex was
 391 developed over the West Shoal (0.5-1 km). Meanwhile, an anticlockwise circulation
 392 with smaller vortex intensity was developed in the region of 1-2km from the western
 393 shore. Another clockwise circulation was developed over the East Shoal. When the
 394 estuary became deepened in 2010, the distribution of the lateral circulation was similar

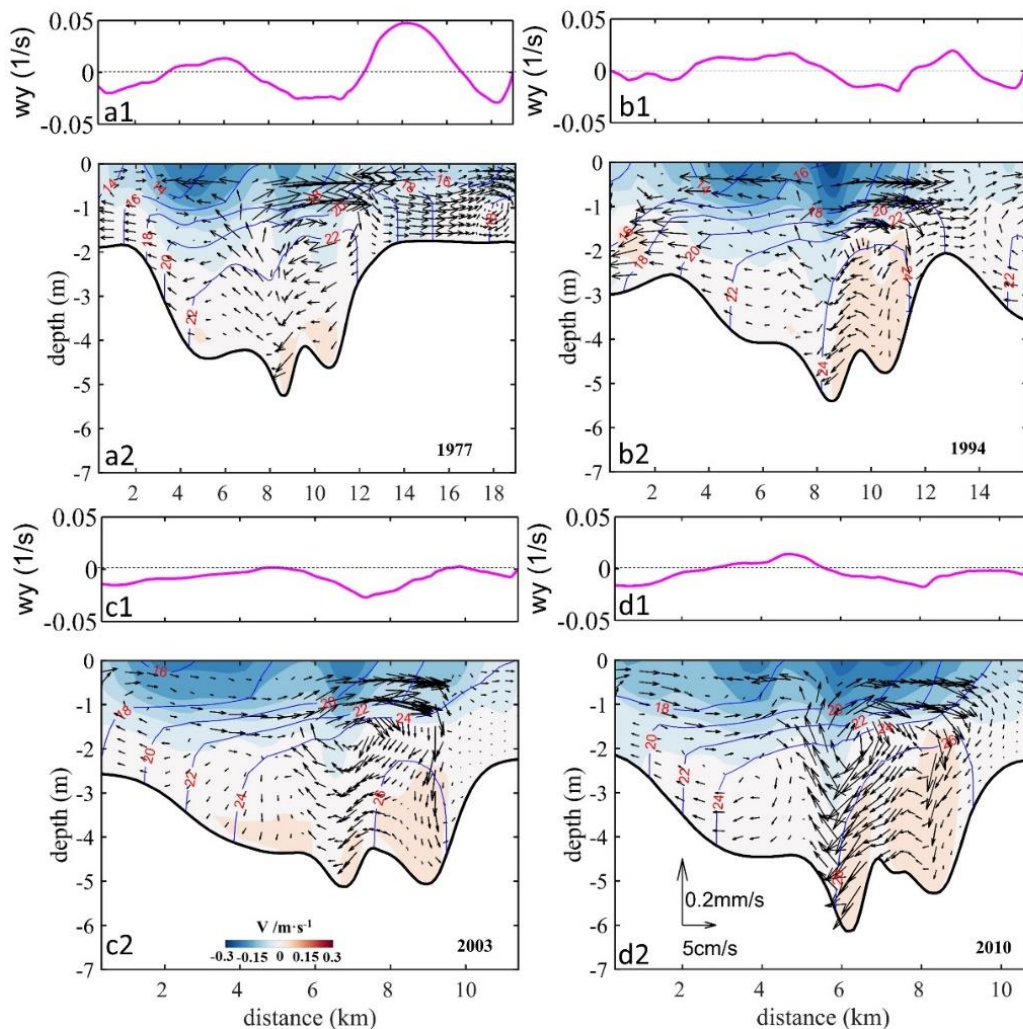
395 to that in 1977, but the vortex intensity increased significantly to about 2-4 times that
 396 of 1977.



397
 398 Fig. 5. The tidally-averaged (from March 10th 00:00 to 11th 00:00 (25h)) lateral circulation
 399 and isohalines (blue lines) at Sec. B1 in 1977(a2), 1994(b2), 2003(c2), and 2010(d2). The
 400 starting point of the X-axis is Point C in Fig. 2d. w_y is the longitudinal vorticity at Sec. B1 in
 401 1977(a1), 1994(a2), 2003(a3), and 2010(a4). The arrows indicate the magnitude of lateral flow
 402 and vertical flow per unit length: 10 cm/s and 1.5 mm/s, respectively. There are more model
 403 grid points than arrows (horizontal resolution: 68m-180m).
 404

405 Figure 6 shows the changes in lateral circulation at Sec. B2. With the decrease of
 406 estuary width, the salinity increased in the cross-section over the years. There
 407 developed a clockwise circulation at the right of the deep channel in 1977 and 1994.
 408 This clockwise vortex was seen to move westward from 2003 on. The spatial extent of

409 the clockwise circulation in the deep channel increased significantly over time.
 410 Clockwise vortices developed over the East Shore from 1977 to 2010, but their intensity
 411 became weaker since 2003. In 1977 and 1994, the distance between the deep channel
 412 and the East Shore was greater than 2 km which was sufficient for accommodating
 413 clockwise vortices. From 2003 on, the accommodation space at the East Shore became
 414 limited and restricted the full development of the clockwise vortex. Over the West
 415 Shoal, the lateral circulation pattern showed an anticlockwise circulation in 1977 and
 416 1994. However, since 2003, the lateral circulation over the West Shoal began to develop
 417 a two-cell pattern, with an anticlockwise gyre at the surface and a clockwise one near
 418 the bottom. The clockwise cell developed well in 2010.



419
 420 Fig. 6. The tidally-averaged (from March 10th 00:00 to 11th 00:00 (25h)) lateral circulation
 421 and isohalines (blue lines) at Sec.B2 in 1977(a2), 1994(b2), 2003(c2), and 2010(d2). The
 422 starting point of the X-axis is Point E in Fig. 2d. w_y is the longitudinal vorticity at Sec. B2

423 in 1977(a1), 1994(a2), 2003(a3), and 2010(a4). The arrows indicate the magnitude of lateral
424 flow and vertical flow per unit length: 5 cm/s and 0.2 mm/s, respectively. There are more model
425 grid points than arrows (horizontal resolution: 64m-316m).

426 As a whole, over the study period, the longitudinal estuarine circulation continued
427 to increase, whereas the lateral circulation experienced varying changes at different
428 cross-sections. At the upstream cross-section (B1), when the estuary narrowed, the
429 original pattern of two-cell vortices with opposite polarity was disrupted. However, it
430 was amplified in 2010 when the water depth was increased. At the cross-section in the
431 middle of the estuary (B2), a similar two-cell pattern was developed. However, in 2003
432 and 2010, the single cell at the West Shoal was split into two cells: an anticlockwise
433 cell at the surface and a clockwise cell at the lower part.

434

435 **3.4 Relationship between the changes in the intensity of estuarine circulation and** 436 **the changes in topography**

437

438 To further quantitatively identify the influence of topographic changes on the
439 estuarine circulation, we calculated the changes in the intensity of estuarine circulations
440 in the longitudinal and lateral directions. The magnitude of estuarine circulation in the
441 longitudinal section was used to represent the intensity of the longitudinal estuarine
442 circulation (Chen and Sanford, 2009). The method was to subtract the subtidal
443 longitudinal velocity of the bottom layer from that on the surface layer. The magnitude
444 of the vorticity in the cross-sections was used to represent the intensity of the lateral
445 circulation (Becherer et al. 2015), and is expressed as:

$$446 \quad w_y = \partial w / \partial x - \partial u / \partial z \quad (2)$$

447 where, w_y is the longitudinal vorticity in the cross-sections. w and u are the
448 currents in the vertical and lateral directions, respectively. $\partial w / \partial x$ is small and can be
449 ignored, therefore, formula (2) can be simplified as:

$$450 \quad w_y = -\partial u / \partial z \quad (3)$$

451 when w_y is positive, the lateral circulation is an anticlockwise vortex, conversely,

452 when w_y is negative, the lateral circulation is a clockwise vortex.

453 The results of the averaged intensity of estuarine circulation along Sec. A and the
 454 averaged intensity of vorticity at the cross-sections are listed in Table 4.
 455 Table 4. The changes of width and depth (the maximum depth), area (cross-section area), w-to-
 456 d, narrowing rate, deepening rate, and the intensity of circulations (w-to-d: width-to-depth ratio;
 457 narrowing rate: the ratio of the difference of cross-section widths between two years divided
 458 by the width in the earlier year; deepening rate: the ratio of the difference of water depth in the
 459 cross-section between the corresponding two years divided by the earlier depth. A positive
 460 narrowing rate indicates that the estuary is narrowed; a positive deepening rate indicates that
 461 the estuary is deepened.)
 462

		time	1977/03	1994/03	2003/03	2010/03
Sec.B1	width (km)		5.56	2.25	2.26	2.14
	depth (m)		7.58	8.76	8.50	13.73
	w-to-d		734	257	266	156
	area (km ²)		0.0468	0.0213	0.0207	0.0256
	narrowing rate		\	59.50%	-0.44%	5.30%
	deepening rate		\	15.58%	-2.95%	61.47%
Sec.B2	width (km)		18.97	15.77	11.40	10.76
	depth (m)		5.25	5.40	5.12	6.13
	w-to-d		3610	2920	2230	1760
	area (km ²)		0.0849	0.303	0.0647	0.0646
	narrowing rate		\	16.87%	27.71%	5.61%
	deepening rate		\	2.86%	-5.19%	19.73%
circulation intensity	longitudinal	Sec. A	0.0274	0.0428	0.0483	0.0594
	lateral	Sec. B1	0.0111	0.0146	0.0130	0.0278
		Sec. B2	0.0493	0.0460	0.0465	0.0425

463
 464 Table 4 indicates that the longitudinal estuarine circulation intensity increased with
 465 the estuary narrowing, and was largest (0.0594 m/s) in 2010.

466 The lateral circulation intensity varied in different cross-sections. For Sec.B1, it
 467 increased gradually when the estuary deepened (from 1994 to 2010). When the
 468 deepening rate reached the maximum (61.47%) in 2010, the lateral circulation intensity
 469 reached the maximum as well. The intensity of lateral circulation increased when the
 470 estuary deepened and narrowed (from 1977 to 1994, and from 2003 to 2010), but it
 471 decreased when the estuary shallowed and narrowed (from 1994 to 2003). For Sec.B2,
 472 the intensity of lateral circulation decreased when the estuary deepened and narrowed
 473 (from 1977 to 1994, and from 2003 to 2010). However, this trend was altered when the

474 estuary entered into the “narrowing and shallowing period”, with the deepening rate
 475 being -5.19%. It indicates that changes in water depth were the dominant factors
 476 affecting the lateral circulation intensity.

477 In general, the relationship between the longitudinal estuarine circulation intensity
 478 and the estuary width showed a monotonic decrease, while that between the
 479 longitudinal estuarine circulation intensity and the water depth is a monotonic increase,
 480 but the lateral circulation intensity seemed to have no simple linear relationship with
 481 the topographic change.

482

483 **4. Discussion**

484

485 **4.1 Contribution of momentum terms to the variation of the longitudinal** 486 **estuarine circulation**

487

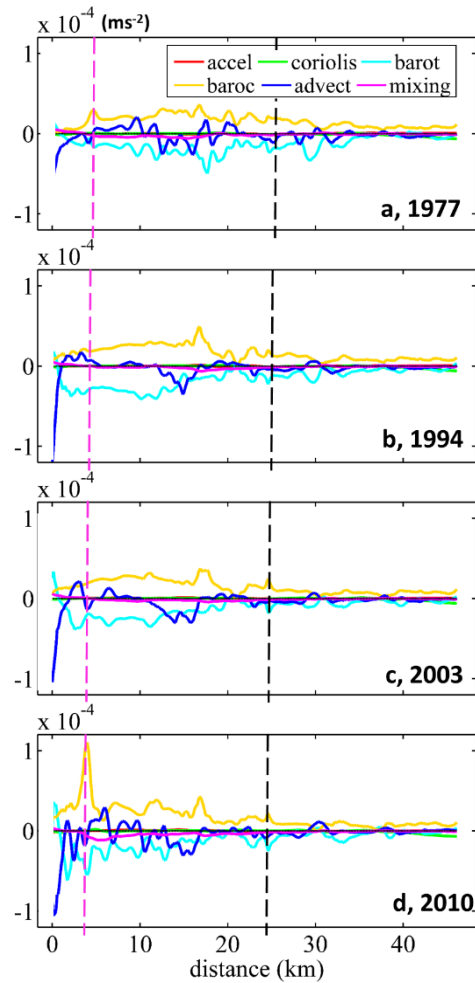
488 To explain the change in the longitudinal estuarine circulation intensity, we
 489 conducted a diagnostic study by examining the changes in terms of the momentum
 490 balance equations. We calculated each term of the momentum equation in the
 491 longitudinal direction in the tidally averaged timescale:

$$492 \quad \underbrace{\frac{\partial v}{\partial t}}_{\text{local acceleration}} = \underbrace{fu}_{\text{coriolis}} - \underbrace{g \frac{\partial \eta}{\partial y}}_{\text{barotropic pressure}} - \underbrace{\frac{gz}{\rho_0} \frac{\partial \rho}{\partial y}}_{\text{baroclinic pressure}} - \underbrace{\left(u \frac{\partial v}{\partial x} + v \frac{\partial v}{\partial y} + w \frac{\partial v}{\partial z} \right)}_{\text{advection}} + \underbrace{\frac{\partial}{\partial z} \left(A_v \frac{\partial v}{\partial z} \right)}_{\text{vertical friction}}, \quad (4)$$

493 By comparing the changes in each term and linking them with the characteristics
 494 of morphological evolution, we explain the response of the longitudinal estuarine
 495 circulation to bathymetric change in the perspective of momentum balance. Though the
 496 change in an individual momentum term in Eq. 4 can not represent the change in the
 497 longitudinal estuarine circulation as a whole, it can reflect the change in the
 498 corresponding component for the estuarine circulation (Cheng, 2013). For example, an
 499 increase or decrease in the baroclinic pressure gradient force can reflect the change in
 500 the gravitational circulation, and the change in the advection term is representative of
 501 the change in tidal rectification. In the following, we present the vertically averaged
 502 values for these different terms along the longitudinal section in different years. It

503 should be noted that the friction term consists of a component of the tidally mean eddy
504 viscosity multiplied by the tidally mean vertical current shear, and a component of the
505 correlation between eddy viscosity and vertical current shear, which is referred to as
506 the tidal straining (Simpson et al., 1990).

507 Figure 7 shows that during the neap tide, the baroclinic pressure gradient force
508 was balanced by barotropic gradient force, friction, and advection term in each year.
509 This is different from the classic estuarine momentum balance (Pritchard, 1956) but
510 consistent with the recent understanding of estuarine physics (Geyer and MacCready,
511 2014). The Coriolis force is quite small as both the latitude of the HE and the residual
512 current are small. The high value of the baroclinic term was observed to shift upstream
513 over time. As the baroclinic term is the multiplication of the salinity gradient and water
514 depth, the changes in this term over years can be induced by the change in water depth
515 and/or the salinity gradient. It can be seen from Fig. 4 that north of the null point, the
516 salt intrusion gradually moved towards the bayhead with the estuary narrowing, thus
517 increasing the salinity gradient there. In the meantime, the upstream water depth was
518 increased due to channel dredging, particularly in 2010. Therefore, the increase of the
519 baroclinic term was caused by both the increases in water depth and salinity gradient.
520 Although the barotropic term contributed a lot to the momentum balance, it did not
521 change obviously with the morphological evolution. The advection term at Sec. B1
522 increased slightly with the estuary narrowing, especially in the deepening part of the
523 channel in 2010. The friction term was larger in 2010 than in other years, because the
524 salt intrusion increased the vertical shear of the longitudinal current at Sec. B1.
525 Nevertheless, the increase in friction term was much smaller than that of the baroclinic
526 term. Chant et al. (2018) attributed the increase in exchange flow to the increase in
527 along-channel salinity gradient and/or a reduction in vertical mixing by deepening, but
528 in our case, the increase in baroclinic term was dominant and the change in vertical
529 mixing even posed a reversed effect.

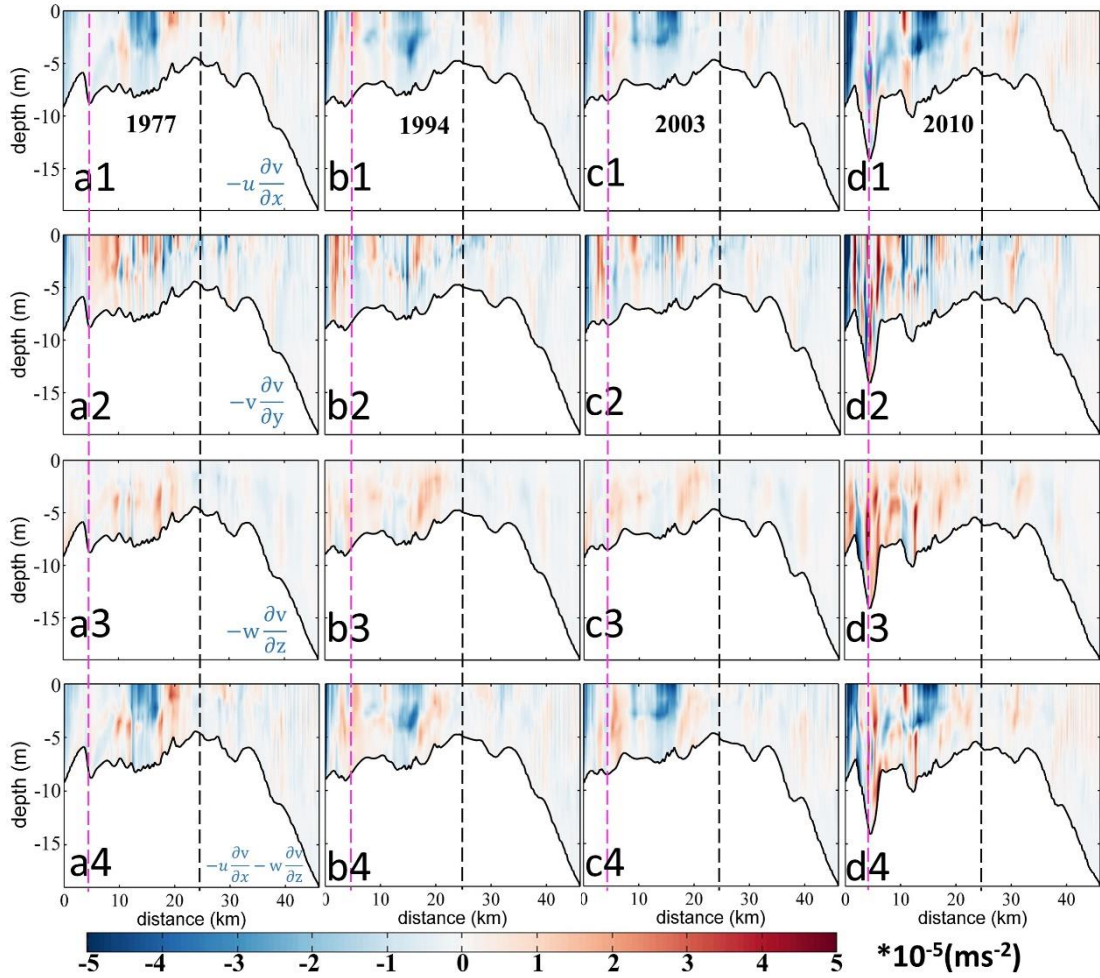


530

531 Fig. 7. Patterns of the tidally-averaged longitudinal momentum terms during neap tide (from
 532 March 10th 00:00 to 11th 00:00 (25h)) at Sec. A in 1977(a), 1994(b), 2003(c), and 2010(d).
 533 The starting point of the X-axis is Point A in Fig. 1b. “accel” in legend: local acceleration term
 534 (the 25h average rate of change of longitudinal flow); “barot” in legend: the barotropic pressure
 535 gradient force; “baroc” in legend: the baroclinic pressure gradient force.

536

537 To further identify the changes in different terms, the advection term was divided
 538 into lateral (X-direction), longitudinal (Y-direction), and vertical (Z-direction)
 539 advection terms (Fig. 8). It is worth noting that the sum of the advection terms in X
 540 and Z directions represents the effect of the lateral circulation.



541

542 Fig. 8. Patterns of the tidally-averaged longitudinal momentum terms during neap tide (from
 543 March 10th 00:00 to 11th 00:00 (25h)) at Sec. A. (a1-d1): The advection in the X direction,
 544 $-u \frac{\partial v}{\partial x}$. (a2-d2): The advection in the Y direction, $-v \frac{\partial v}{\partial y}$. (a3-d3): The advection in the Z
 545 direction, $-w \frac{\partial v}{\partial z}$. (a4-d4): The sum of the advection terms in X and Z directions. 1977, 1994,
 546 2003, and 2010 cases are in the first, second, third, and fourth columns, respectively. The pink
 547 and black dotted lines represent the location of Sec.B1 and Sec.B2, respectively. The starting
 548 point of the X-axis is Point A in Fig. 1b.

549

550 Compared to the results in other years, the advection terms (in both longitudinal
 551 and lateral all direction), increased significantly in 2010 (Figs. 8a1-d4), following the
 552 deepening and narrowing of the estuary. Generally, the lateral and vertical advection
 553 competes against each other, and their additive effect is to generate a circulation similar

554 to the gravitational circulation. This effect was stronger in 2010 than in other years
 555 (Figs. 8a4-d4).

556 Overall, from 1977 to 2010, the baroclinic forcing, the friction, and the advection
 557 terms increased obviously along the Sec. A. The maximum longitudinal estuarine
 558 circulation in 2010 was caused by the increase in the pressure gradient force and the
 559 advection term, especially the baroclinic forcing.

560

561 **4.2 Analysis of the streamwise vorticity balance for the lateral flow**

562

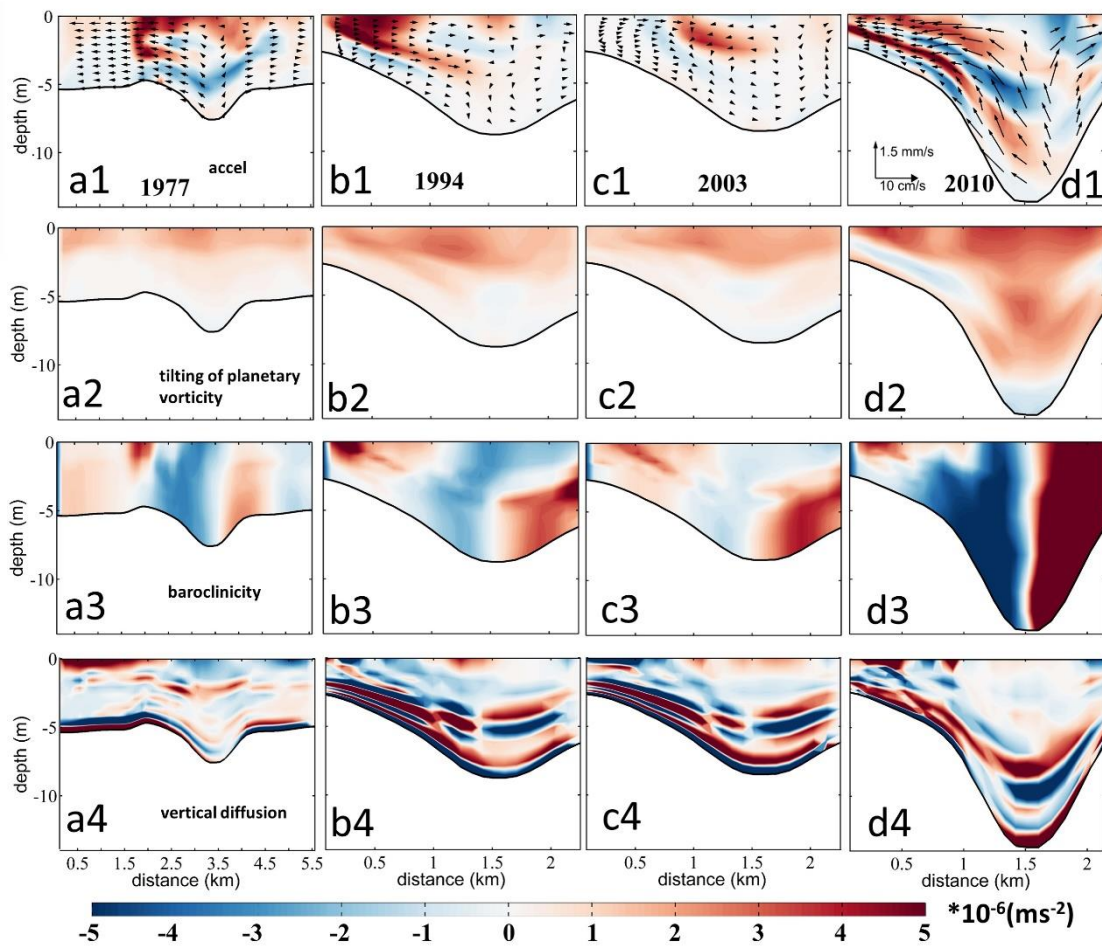
563 In order to reveal the contribution of the vertical shear of the along-channel flow,
 564 the lateral salinity gradient, and the vertical diffusion to changes in the lateral
 565 circulation, we examine the changes in terms of the streamwise vorticity transport
 566 equation (Li et al., 2014):

$$567 \quad \frac{dw_y}{dt} = \underbrace{-f \frac{\partial v}{\partial z}}_{\text{tilting of planetary vorticity}} \underbrace{-g\beta \frac{\partial S}{\partial x}}_{\text{baroclinicity}} \underbrace{+ \frac{\partial^2}{\partial z^2} (K_V w_y)}_{\text{vertical diffusion}} \underbrace{+ \frac{\partial^2}{\partial x^2} (K_H w_y)}_{\text{horizontal diffusion}}, \quad (5)$$

568 In the right side of Eq. 5, the first term represents the tilting of the planetary
 569 vorticity by vertical shear in the along-channel flow, the second term is the baroclinicity
 570 caused by the lateral salinity gradient, the third term is the vertical diffusion, and the
 571 fourth term is the horizontal diffusion, which is typically two orders of magnitude
 572 smaller than the vertical diffusion term. Therefore, we only show the acceleration and
 573 first three right-hand-side terms in Fig. 9.

574 Figure 9 shows that the changes of baroclinic term caused by the water depth
 575 change dominated the changes in the lateral circulation at Sec. B1. The baroclinic term
 576 in the deep channel was generally negative at the left side of the channel, and it
 577 increased significantly in 2010, about 2-3 times the value in 1977. The baroclinic term
 578 with positive values occurred at the West Shoal over the study period, but the areal
 579 extent occupied by the positive values decreased gradually, with its magnitude
 580 increased obviously in 1994 when the narrowing rate was the largest. A negative
 581 baroclinic term appeared at the bottom of the West Shoal, indicating that the changes

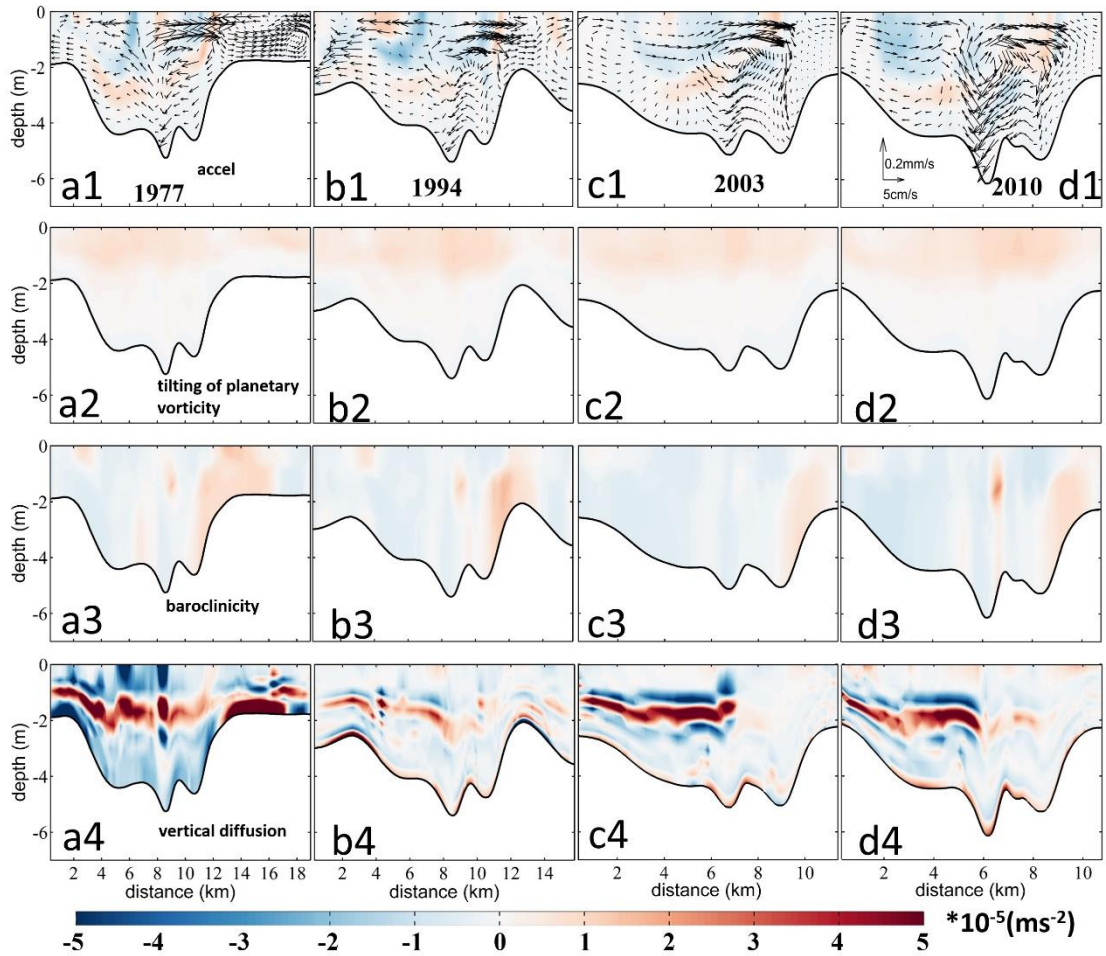
582 in water depth can lead to changes in the pattern and magnitude of the baroclinic term,
 583 which was mainly caused by the changes in the salt intrusion. The tilting of the
 584 planetary vorticity term increased with the estuary narrowing, the greater increase in
 585 2010 was mostly caused by the depth change. The pattern of the vertical diffusion term
 586 changed significantly in 1977 and 1994, especially at the surface and the bottom layers
 587 of the West Shoal, indicating that it was the changes in width that altered the vertical
 588 diffusion term.



589

590 Fig. 9. Patterns of the tidally-averaged streamwise vorticity equation terms during neap tide
 591 (from March 10th 00:00 to 11th 00:00 (25h)) at Sec. B1. (a1-d1): The local acceleration term
 592 (the 25h average rate of change of the longitudinal vorticity). (a2-d2): The tilting of planetary
 593 vorticity term. (a3-d3): The baroclinic term. (a4-d4): The vertical diffusion term. The cases in
 594 1977, 1994, 2003, and 2010 are in the first, second, third, and fourth columns, respectively. The
 595 starting point of the X-axis is Point C in Fig. 2d. For viewing purposes, the acceleration term is
 596 multiplied by 5. The block arrows in a1-d1 represent the distribution of lateral circulation.

597



598

599 Fig. 10. Patterns of the tidally-averaged streamwise vorticity equation terms during neap tide
 600 (from March 10th 00:00 to 11th 00:00 (25h)) at Sec. B2. (a1-d1): The local acceleration term
 601 (the 25h average rate of change of the longitudinal vorticity). (a2-d2): The tilting of planetary
 602 vorticity term. (a3-d3): The baroclinic term. (a4-d4): The vertical diffusion term. The cases in
 603 1977, 1994, 2003, and 2010 are in the first, second, third, and fourth columns, respectively. The
 604 starting point of the X-axis is Point E in Fig. 2d. For viewing purposes, the acceleration term is
 605 multiplied by 5. The block arrows in a1-d1 represent the distribution of lateral circulation.
 606

607 From Fig. 10, the change in the tilting of the planetary vorticity at Sec. B2 was
 608 analogous to that at Sec. B1. The baroclinic term did not change much, because the
 609 changes in water depth were smaller in this section. The clockwise circulation over the
 610 West shoal increased as the estuary deepened in 2010, because the baroclinic term was
 611 larger with the increase of salt intrusion and vertical salinity gradient near Sec. B2. The
 612 vertical diffusion of the vorticity was overall negative, indicating its effect in dissipating
 613 the vorticity. The vertical diffusion term was larger than the baroclinic term, especially

614 in the middle water, which was inconsistent with the conclusion that the baroclinic term
615 is the most important one in the lateral circulation (Li et al., 2014). The reason may be
616 that in our study site, the vertical mixing was strong as the estuary became shallow.
617 However, the existence of a pycnocline greatly weakened the momentum exchange
618 between the upper and lower layers: above the pycnocline, the tilting of the planetary
619 vorticity was dominant; whereas, under the pycnocline, the baroclinic term was
620 dominant. The decrease of the estuary width changed the magnitude and pattern of the
621 vertical diffusion term: the area with a large positive value disappeared at the bottom
622 of the East Shoal and the magnitude of the negative value decreased greatly at the
623 eastern end of the section. It indicates that in a shallow estuary, the vertical diffusion
624 term caused by the width change is also important.

625 In Summary, the tilting of the planetary vorticity increased with the decrease of
626 width or with the increase of water depth. The variation of estuary width was
627 responsible for the changes in the vertical diffusion term, and the changes in water depth
628 were responsible for the changes in the baroclinic term. The increase of the longitudinal
629 estuary circulation can increase the baroclinic term at the cross-sections by increasing
630 the salinity gradient near the cross-sections, as mainly occurred in the periods of the
631 estuary deepening. The deepening rate of Sec.B1 was the fastest (61%) in 2010, which
632 led to the strongest lateral circulation in 2010. The lateral circulation intensity decreased
633 when the estuary narrowed in 2003 due to the decreased baroclinic term. In addition,
634 the shallowing was the main reason for the pattern change of the lateral circulation at
635 Sec.B2. At Sec. B2, the narrowing rate was the fastest in 2003, and the adjustment of
636 the vertical diffusion term resulted in an increased lateral circulation from 1994 to 2003.
637 The decrease of the clockwise circulation at the East Shoal was mainly related to the
638 adjustment of the vertical diffusion term to the baroclinic term.

639

640 **4.3 Comparison to theoretical results and other estuaries influenced by human** 641 **interventions**

642

643 The longitudinal estuarine circulation is generated by the river discharge, Stokes
644 return flow, longitudinal baroclinic pressure gradient force, tidal straining, and
645 advection (Geyer and Maccready, 2014). The HE features a microtidal tidal regime
646 (tidal range less than 1.5 m), and the component generated by the baroclinic pressure
647 gradient, i.e., the gravitational circulation, would be a primary part of the longitudinal
648 estuarine circulation. The convergent geometry makes it susceptible to the residual flow
649 induced by the longitudinal advection (Burchard et al., 2014). However, as shown in
650 Fig. 8, not only the longitudinal advection but also the lateral advection plays the
651 important role in generating the estuarine circulation in the HE.

652 With channel deepening and width narrowing in the HE, the gravitational
653 circulation was increased by the increased baroclinic pressure gradient force. Based on
654 Geyer's research (2010), the gravitational circulation can be simplified to:

$$655 \quad v_g = a_1(\beta g s_0 R w_0 h_0)^{1/5} U_0^{2/5} w^{-2/5} h^{-1/5}, \quad (6)$$

656 in which w_0 and h_0 is the width and depth at the estuary mouth, respectively. It
657 indicates that the gravitational circulation is inversely related to the water depth and
658 width in the estuary, with a weaker dependence on the water depth. In Chant et al.
659 (2018), the gravitational circulation is completely unrelated to the water depth in their

660 equation (2), which is $v_g \propto \left(\frac{g' R}{w}\right)^{\frac{1}{3}}$, in which the g' is the reduced gravity acceleration.

661 This seems to contradict the situations occurring in many estuaries, such as in the Coos
662 Bay (Eidam et al., 2020), Tampa Bay (Zhu et al., 2015), Changjiang Estuary (Zhu,
663 2018), Ems estuary (Van Maren et al., 2015), Hudson Estuary (Ralston and Geyer,
664 2019), and Newark Bay of the Delaware estuary (Chant et al., 2018). In all these
665 estuaries, the gravitational circulation demonstrated an increase with the deepening of
666 the channel. It suggests that the changes in gravitational circulation vary in different
667 parts of the estuary and the longitudinal salinity gradient may not catch up with the
668 change in water depth in the analytical solution, as proposed by Chant et al. (2018) and
669 Ralston and Geyer (2019). In our study site, the salinity gradient at the upstream part

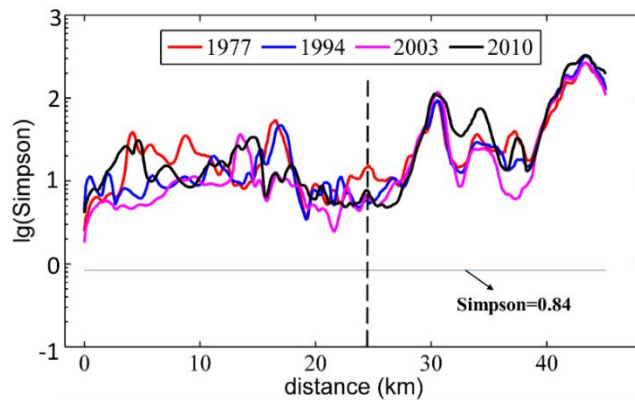
670 of the longitudinal section was increased owing to an enhanced salt intrusion where
 671 water depth increased, which led to an increased gravitational circulation in the upper
 672 HE (Fig. 4).

673 The tidal straining-induced estuarine circulation is another important component of
 674 longitudinal estuarine circulation. The straining-induced circulation is the covariance
 675 of the eddy viscosity and the vertical shear of the longitudinal flow (ESCO) in a tidal
 676 cycle and is included in the term of internal friction. Cheng et al. (2010) have indicated
 677 that ESCO-induced flow dominates the gravitational circulation in periodically
 678 stratified estuaries with strong tides, having the same structure as the gravitational
 679 circulation. It has the same order of magnitude in weakly stratified estuaries with
 680 moderate tides, and is less important in highly stratified estuaries with weak tides, even
 681 with a reversed structure with the gravitational circulation. As indicated by Becherer et
 682 al. (2015), the strength of the straining-induced circulation is dependent on the Simpson
 683 number (or the horizontal Richardson number). The Simpson number is expressed as:

$$684 \quad S_i = g\beta \frac{dS}{dy} \frac{h^2}{u_*^2}, \quad (7)$$

685 in which u_* is the bottom friction velocity, represented by $u_* = \sqrt{C_d}U_t$, where C_d is
 686 the bottom friction coefficient and U_t is the tidal velocity amplitude.

687 When S_i is larger than 0.84, the water column is in a persistent stratified situation,
 688 and the straining-induced circulation becomes weaker. We calculated the S_i along the
 689 longitudinal section in different years and depict them in Fig. 11.



690

691 Fig. 11. Distribution of the Simpson number in different years along the longitudinal section.
692 The Y-axis represents the logarithm of the S_i . The black dotted line represents the location of
693 the null point.

694 It indicates that along the longitudinal section, the S_i number was mostly above
695 the criterion of 0.84, showing that the straining-induced circulation is not significant.
696 The S_i number was the smallest in 2003 and the largest in 2010. It indicates that with
697 the narrowing and deepening of the HE, the straining-induced circulation became
698 weaker. This is consistent with Burchard et al. (2014) and Schulz et al. (2015). It
699 indicates that with the human interventions, the straining-induced circulation became
700 less important in the longitudinal estuarine circulation.

701 For the advection-induced longitudinal estuarine circulation, we noted that the
702 longitudinal and vertical advection terms were smaller than the lateral advection. Based
703 on Cheng and Valle-Levinson (2009), the lateral advection-induced longitudinal
704 circulation is proportional to the ratio of $h/(wK_m)$, where w is the width, and K_m is
705 the eddy viscosity. It shows that in a narrower and deeper estuary, the lateral advection
706 has a larger effect in influencing the longitudinal estuarine circulation. Lerczak and
707 Geyer (2004) also showed that the effect of the lateral advection on longitudinal
708 circulation is stronger for narrower estuaries. Our results show that with the narrowing
709 and deepening of the estuary, not only the lateral advection but also the longitudinal
710 advection has great influences on the longitudinal estuarine circulation.

711

712 **4.4 The possible future development of the estuarine circulation and its**

713 **implications**

714

715 The pattern of lateral circulation during the dry season in the HE experienced a
716 dramatic change from 2003 to 2010 in the West Shoal at Sec. B2, from an under-
717 developed circulation structure to a complete clockwise vortex in 2010. This transition
718 was associated with the increase in lateral salinity gradient, the increase in longitudinal
719 bottom landward flow, and a decrease of friction by the increased water depth and
720 stratification.

721 The mechanisms for the lateral circulation during the wet season have been
722 revealed by Chen et al. (2020b), who showed that it was primarily driven by the
723 barotropic process, i.e., the water elevation gradient, and thus by the intensity of the
724 ebb jet. Different from the wet season when the river discharge was higher, the lateral
725 circulation in the dry season was more affected by the baroclinic effect. We speculate
726 that, with the narrowing and deepening of the estuary, the lateral circulation will be
727 enhanced even in the wet season accompanied by the strengthened ebb jet in the deep
728 channel.

729 In the HE, the channel underwent siltation, and sediment was carried from the
730 channels to side banks by the lateral circulation, making the estuary overall shallower
731 in 2003. In 2005, dredging of the channel increased the channel depth (Luo, 2010), and
732 increased the longitudinal estuarine circulation, though the lateral circulation decreased
733 slightly by the smaller rate of convergence. If reclamation is less frequent than in the
734 last century, and the channel dredging continues, then circulation in the HE will keep
735 increasing as the water depth increases, and thus a positive feedback exists. However,
736 as revealed in Eq. (6) and Eq. (2) in Chant et al. (2018), with the increase in salt
737 intrusion, the longitudinal salinity gradient will decrease, showing negative feedback.
738 Moreover, Schulz et al. (2015) noted that estuarine circulation exhibited a distinct
739 maximum in medium-wide channels by comparing estuarine circulation under different
740 width-to-depth ratios. In our study, as shown in Table 4, the width-to-depth ratio has
741 been decreasing from 1977 to 2010, but the estuarine circulation has been increasing.
742 The difference would be caused by the fact that in our study site, the tidal mixing is not
743 strong enough to generate an effective tidal straining-induced circulation.

744 The changes in the estuarine circulation have important implications for sediment
745 transport and morphological evolution in the HE. With the increase of longitudinal
746 estuarine circulation, the sediment trapping effect is expected to be enhanced, thus more
747 riverine sediment would be trapped inside the estuary. In the meantime, a decrease in
748 lateral circulation would decrease the sediment advection from the channel to the West

749 Shoal, which occurred in the wet season and was favorable for the siltation in the West
750 Shoal (Chen et al., 2020b).

751 Being a micro-tidal partially mixed estuary with standing tidal wave, the estuarine
752 circulation in HE is stronger during the neap tide than during the spring tide. After
753 analyzing the circulation during spring tide, we found the longitudinal circulation
754 reached maximum in 2010 when the water depth was the largest. Similar to the
755 phenomenon during the neap tide, the longitudinal circulation was dominated by the
756 increase in the baroclinicity. However, the changes in the lateral circulation were more
757 complicated than that during the neap tide. In addition to the baroclinicity, the change
758 in vertical diffusion caused by the width change also played an important role. The
759 changes in lateral circulation at the upstream section (Sec. B1) were mostly controlled
760 by the changes in the baroclinicity. On the other hand, the changes in lateral circulation
761 at the downstream section (Sect. B2) were mainly controlled by the changes in the
762 vertical diffusion.

763 In this study, the model used was only driven by river discharge and tides, without
764 considering the effects of winds, waves, sea level rise, and other upstream flows into
765 the estuary. Future work could incorporate the above factors to improve the model's
766 accuracy. Sea level rise can increase the total water depth and inundate more intertidal
767 areas. It has an effect similar to that of channel deepening, to increase the salt intrusion
768 and estuarine circulation. The river flow will be generally decreased in the PRD due to
769 global warming and northward shift of the climate zone. With a decrease of the river
770 discharge, the salt intrusion will be increased and thus the salinity gradient will be
771 decreased, resulting in a weakened estuarine circulation in the HE. For the salinity at
772 the offshore boundary, we are not certain whether it will be increased or decreased. It
773 is influenced by the rain and evaporation, and the large-scale salt transport in the South
774 China Sea. If it increases, the salinity gradient in the HE will be increased, and the
775 estuarine circulation will be enhanced therefore. And vice versa.

776 Definitely, the estuary has undergone natural changes in 40+ years, such as the
777 changes in river inflow, offshore boundary conditions. However, our focus is on the

778 impact of changes in bathymetry on the estuarine circulation, we leave the effect of
779 other factors for future investigation. It should be noted that our model simulations are
780 not used to reproduce exactly the historical evolution, but to reveal the underlying
781 dynamics.

782

783 **5. Conclusion**

784

785 This study investigated the morphological evolution of the HE from 1977 to 2010
786 using ArcGIS and remote sensing. It was noted that the West Channel of the HE
787 disappeared, causing the morphological pattern to change from “two channels and
788 three shoals” gradually to “one channel and two shoals” throughout the years. Due to
789 the reclamation and development of salt marshes along the estuarine banks, the estuary
790 has been experiencing continuous narrowing. Meanwhile, channel dredging has
791 deepened the estuary over the study period. It had been revealed that the sediment
792 transport pattern changes in response to the changes in river discharge and tidal mixing
793 (Gong et al., 2014). Generally, there exists a sediment convergence zone in the middle
794 of the estuary, and the riverine sediment is trapped inside the estuary to form a
795 turbidity maximum. Our results indicate that the intensity of the longitudinal estuarine
796 circulation kept increasing as the estuary width continued to decrease. The trend of the
797 lateral circulation intensity altered (decreased at Sec. B1 and increased at Sec. B2)
798 when the estuary shallowed (from 1994 to 2003).

799 The changes in the longitudinal estuarine circulation were dominated by the
800 changes in the baroclinic pressure gradient force and advection. As the estuary was
801 narrowing and deepening, the pressure gradient force and advection term (especially
802 the longitudinal advection term) increased, which increased the longitudinal
803 circulation. The change in lateral circulation intensity was mainly caused by the
804 change of the vertical shear of the longitudinal subtidal flow, the lateral salinity
805 gradient, and the vertical dissipation term. The changes in water depth were the

806 dominant factor affecting lateral circulation intensity. The increase of water depth
807 enhanced the longitudinal circulation and the lateral circulation of the upstream cross-
808 section in 2010. The changes in the estuarine circulation have great implications for
809 the sediment transport in the HE, which would be explored in the next step.

810

811 **Data availability**

812 A total of 142G data of 66 images (Table 1) covering the PRD during cloudless days
813 in multiple years (from 1973 to 2018) were downloaded from <http://www.gscloud.cn/>.

814

815 **Author contributions**

816 RuiZhang: Writing - original draft, model runs and analyses. Bo Hong: Writing -
817 review. Lei Zhu: Writing - review. Wenping Gong: Writing - review & editing,
818 Conceptualization, Funding acquisition. Heng Zhang: Visualization, Funding
819 acquisition.

820

821 **Competing interests**

822 The authors declare that they have no conflict of interest.

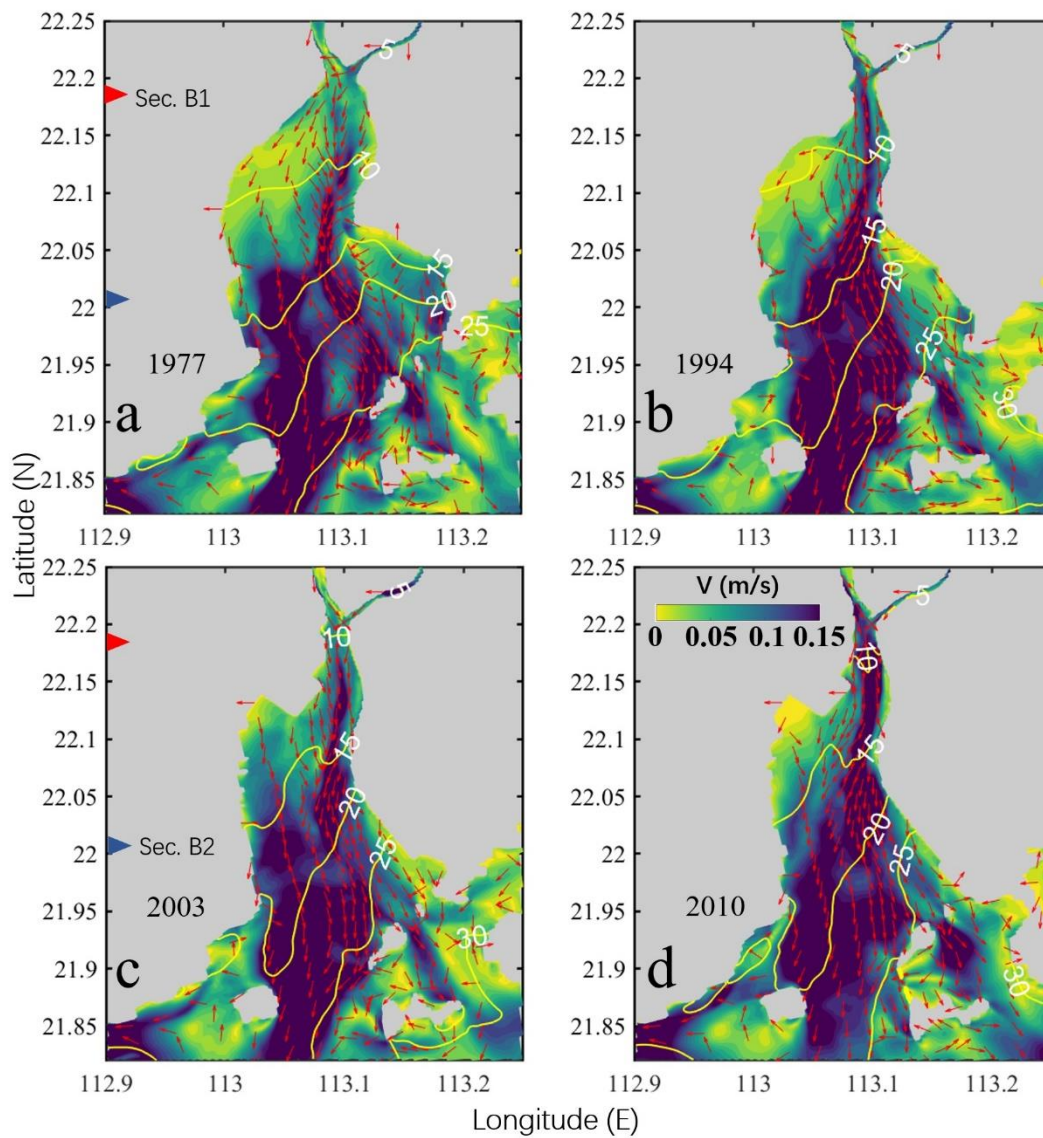
823

824 **Acknowledgments**

825 This research is funded by the National Natural Science Foundation of China [Grant
826 nos. 51761135021, 41506102, 41890851]. We would like to thank the National
827 Aeronautics and Space Administration (NASA) for providing the Landsat remote
828 sensing data. We are very grateful to graduate students in our team from Sun Yat-sen
829 for their help in fieldwork and sediment sample analysis in the indoor laboratory.

830

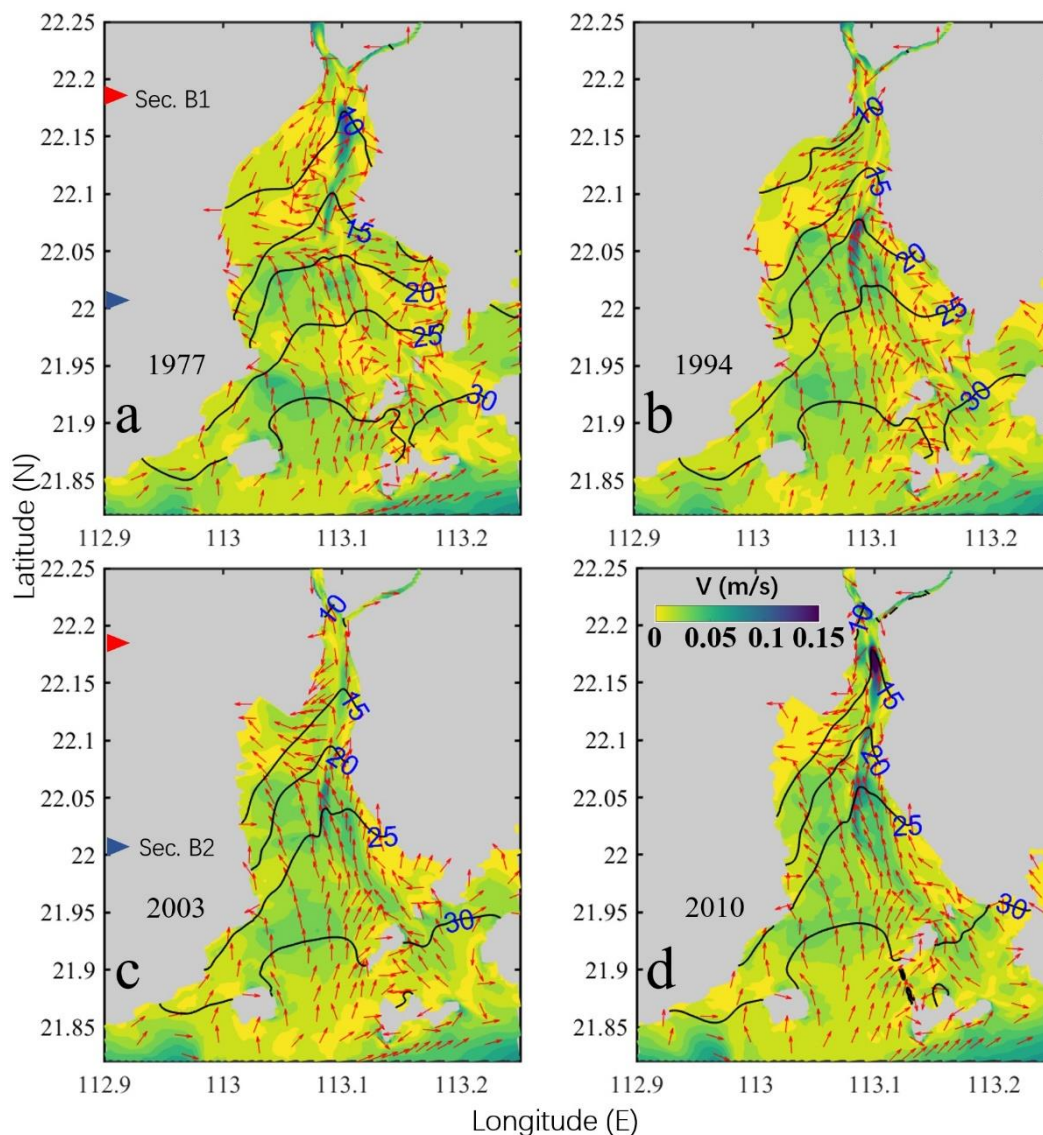
831 **Appendix A**



832

833 Fig. A. 1. Patterns of the tidally and vertically averaged horizontal circulation at the surface
 834 during neap tide (from March 10th 00:00 to 11th 00:00 (25h)) in 1977(a1), 1994(a2), 2003(a3),
 835 and 2004(a4). The magnitude of the current is represented by the color shading, while the
 836 current direction is shown by the arrows. The salinity is depicted by the contour lines. The red
 837 and blue triangles depict the positions of two cross-sections (Sec.B1 and Sec.B2).

838



839

840 Fig. A. 2. Patterns of the tidally and vertically averaged horizontal circulation at the bottom
 841 during neap tide (from March 10th 00:00 to 11th 00:00 (25h)) in 1977(a1), 1994(a2), 2003(a3),
 842 and 2004(a4). The magnitude of the current is represented by the color shading, while the
 843 current direction is shown by the arrows. The salinity is depicted by the contour lines. The red
 844 and blue triangles denote the positions of two cross-sections (Sec.B1 and Sec.B2).

845

846 References

847

848 Ai, B., Zhang, R., Zhang, H., Ma, C. L. and Gu, F. G.: Dynamic process and artificial mechanism of
 849 coastline change in the Pearl River Estuary, *Regional Studies in Marine Science*, 30, 100715, 2019.

850 Amin, M.: On perturbations of harmonic constants in the Thames Estuary, *Geophysical Journal of the*
 851 *Royal Astronomical Society*, 73, 587-603, 1983.

852 Becherer, J., Stacey, M. T., Umlauf, L. and Burchard, H.: Lateral circulation generates flood tide
 853 stratification and estuarine exchange flow in a curved tidal inlet, *J. Phys. Oceanogr.*, 45, 638-656,

854 2015.

855 Burchard, H., Hetland, R. D., Schulz, E. and Schuttelaars, H. M.: Drivers of Residual Estuarine
856 Circulation in Tidally Energetic Estuaries: Straight and Irrotational Channels with Parabolic Cross
857 Section, *J. Phys. Oceanogr.*, 41, 548-570, 2010.

858 Burchard, H., Schulz, E. and Schuttelaars, H. M.: Impact of estuarine convergence on residual circulation
859 in tidally energetic estuaries and inlets, *Geophys. Res. Lett.*, 41, 913-919, 2014.

860 Chant, R. J., Sommerfield, C. K. and Talke, S. A.: Impact of channel deepening on tidal and gravitational
861 circulation in a highly engineered estuarine basin, *Estuar. Coast.*, 41, 1587-1600, 2018.

862 Chen, L. H., Gong, W. P., Scully, M. E., Zhang, H., Cheng, W. C. and Li, W.: Axial wind effects on
863 stratification and longitudinal sediment transport in a convergent estuary during wet season, *Journal*
864 *of Geophysical Research: Oceans*, 125, e2019J-e15254J, 2020a.

865 Chen, L. H., Gong, W. P., Zhang, H., Zhu, L. and Cheng, W. C.: Lateral circulation and associated
866 sediment transport in a convergent estuary, *Journal of Geophysical Research: Oceans*, 125, e2019J-
867 e15926J, 2020b.

868 Chen, S. N., Geyer, W. R., Ralston, D. K. and Lerczak, J. A.: Estuarine Exchange Flow Quantified with
869 Isohaline Coordinates: Contrasting Long and Short Estuaries, *J.phys.oceanogr*, 42, 748-763, 2012.

870 Chen, S. N. and Sanford, L. P.: Axial Wind Effects on Stratification and Longitudinal Salt Transport in
871 an Idealized, Partially Mixed Estuary, *J. Phys. Oceanogr.*, 39, 1905-1920, 10.1175/2009JPO4016.1,
872 2009.

873 Cheng, P.: Decomposition of Residual Circulation in Estuaries, *Journal of Atmospheric & Oceanic*
874 *Technology*, 31, 698-713, 2013.

875 Cheng, P. and Valle-Levinson, A.: Influence of lateral advection on residual currents in microtidal
876 estuaries, *J. Phys. Oceanogr.*, 39, 3177-3190, 2009.

877 Cheng, P., Valle-Levinson, A. and De Swart, H. E.: Residual currents induced by asymmetric tidal
878 mixing in weakly stratified narrow estuaries, *J. Phys. Oceanogr.*, 40, 2135-2147, 2010.

879 Chernetsky, A. S., Schuttelaars, H. M. and Talke, S. A.: The Effect of Tidal Asymmetry and Temporal
880 Settling Lag on Sediment Trapping in Tidal Estuaries, *Ocean Dynam.*, 60, 1219-1241, 2010.

881 Dyer, K. R. 1977. Lateral circulation effects in estuaries. *National Academy of Sciences*, p. 22-29.

882 Eidam, E. F., Sutherland, D. A., Ralston, D. K., Dye, B., Conroy, T., Schmitt, J., Ruggiero, P. and Wood,
883 J.: Impacts of 150 Years of Shoreline and Bathymetric Change in the Coos Estuary, Oregon, USA,
884 *Estuar. Coast.*, 1-19, 2020.

885 Fischer, H. B.: Mixing and Dispersion in Estuaries, *Annu. Rev. Fluid Mech.*, 8, 107-133,
886 10.1146/annurev.fl.08.010176.000543, 1976.

887 Geyer, W. R.: Estuarine salinity structure and circulation, *Contemporary issues in estuarine physics*, 12,
888 26, 2010.

889 Geyer, W. R. and Maccready, P.: The Estuarine Circulation, *Annu. Rev. Fluid Mech.*, 46, 175-197, 2014.

890 Geyer, W. R. and Nepf, H.: Tidal pumping of salt in a moderately stratified estuary, *Coastal and estuarine*
891 *studies*, 213-226, 1996.

892 Gong, W. P., Jia, L. W., Shen, J. and Liu, J. T.: Sediment transport in response to changes in river
893 discharge and tidal mixing in a funnel-shaped micro-tidal estuary, *Cont. Shelf Res.*, 76, 89-107,
894 2014.

895 Gong, W. P., Liu, H., Ren, J. and Yu, H. B.: The study of tidal propagation in the Huangmaohai estuary
896 and its underlying mechanisms, *Acta Oceanol. Sin.*, 34, 41-54, 2012.

897 Gong, W. P., Schuttelaars, H. and Zhang, H.: Tidal asymmetry in a funnel-shaped estuary with mixed
898 semidiurnal tides, *Ocean Dynam.*, 66, 637-658, 2016.

899 Huang, T. 2011. Study on abnormal changes of tidal range in the huangmaohai estuary. Guangdong
900 Water Resources and Hydropower, Guangzhou, China.

901 Jia, L. W., Luo, J. and Ren, J.: The analysis of the evolution of a sand bar and its formation in the
902 Huangmao Bay in the Pearl River Delta, *Acta Oceanol. Sin.*, 34, 120-127, 2012.

903 Kjerfve, B., Stevenson, L. H., Proehl, J. A., Chrzanowski, T. H. and Kitchens, W. M.: Estimation of
904 material fluxes in an estuarine cross section: A critical analysis of spatial measurement density and
905 errors 1, *Limnol. Oceanogr.*, 26, 325-335, 1981.

906 Lacy, J. R., Stacey, M. T., Burau, J. R. and Monismith, S. G.: Interaction of lateral baroclinic forcing and
907 turbulence in an estuary, *Journal of Geophysical Research: Oceans*, 108, 1-34,
908 <https://doi.org/10.1029/2002JC001392>, 2003.

909 Lerczak, J. A. and Rockwell Geyer, W.: Modeling the Lateral Circulation in Straight, Stratified
910 Estuaries*, *J. Phys. Oceanogr.*, 34, 1410-1428, 2004.

911 Lesser, G. R., Roelvink, J. V., Van Kester, J. and Stelling, G. S.: Development and validation of a three-
912 dimensional morphological model, *Coast. Eng.*, 51, 883-915, 2004.

913 Li, C. Y. and O'Donnell, J.: Tidally driven residual circulation in shallow estuaries with lateral depth
914 variation, *Journal of Geophysical Research Oceans*, 102, 27915-27929, 1997.

915 Li, M., Cheng, P., Chant, R. J., Valle-Levinson, A. and Arnott, K.: Analysis of vortex dynamics of lateral
916 circulation in a straight tidal estuary, *J. Phys. Oceanogr.*, 44, 2779-2795, 2014.

917 Li, W., Shi, J. Z., Pu, X. and Hu, G. D.: Circulation within curved channel of the north passage in the
918 changjiang river estuary: a vorticity approach, *Oceanologia et Limnologia Sinica*, 48, 682-694, 2017.

919 Li, Y. B. 2019. Numerical simulation of the formation and evolution of the geomorphic characteristics
920 of Huangmao Sea. Dalian University of Technology, Dalian, China.

921 Luo, J. 2010. Cause Analysis of Morphological evolution of Huangmao sea Estuary in the Decade to
922 Century-scale. Sun Yat-sen university, Guangzhou, China.

923 Pritchard, D. W.: Salinity distribution and circulation in the Chesapeake Bay estuarine system.. 1, *Mar.*
924 *Res*, 11, 106-123, 1952.

925 Pritchard, D. W.: The dynamic structure of a coastal plain estuary, *J Marine Res*, 15, 33-42, 1956.

926 Ralston, D. K. and Geyer, W. R.: Response to channel deepening of the salinity intrusion, estuarine
927 circulation, and stratification in an urbanized estuary, *Journal of Geophysical Research: Oceans*,
928 124, 4784-4802, 2019.

929 Salles, P., Valle-Levinson, A., Sottolichio, A. and Senechal, N.: Wind - driven modifications to the
930 residual circulation in an ebb - tidal delta: Arcachon Lagoon, Southwestern France, *Journal of*
931 *Geophysical Research Oceans*, 120, 728-740, 2015.

932 Schulz, E., Schuttelaars, H. M., Gr We, U. and Burchard, H.: Impact of the depth-to-width ratio of
933 periodically stratified tidal channels on the estuarine circulation, *J. Phys. Oceanogr.*, 45, 411804097,
934 2015.

935 Scully, M. E., Geyer, W. R. and Lerczak, J. A.: The Influence of Lateral Advection on the Residual
936 Estuarine Circulation: A Numerical Modeling Study of the Hudson River Estuary, *J. Phys.*
937 *Oceanogr.*, 39, 107-124, 10.1175/2008JPO3952.1, 2009.

938 Scully, M. E., Geyer, W. R. and Lerczak, J. A.: The Influence of Lateral Advection on the Residual
939 Estuarine Circulation: A Numerical Modeling Study of the Hudson River Estuary, *J. Phys.*

940 Oceanogr., 39, 107-124, 10.1175/2008JPO3952.1, 2009.

941 Scully, M., Friedrichs, C. and Brubaker, J.: Control of estuarine stratification and mixing by wind-
942 induced straining of the estuarine density field, *Estuaries*, 28, 321-326, 10.1007/BF02693915, 2005.

943 Simpson, J. H., Brown, J., Matthews, J. and Allen, G.: Tidal straining, density currents, and stirring in
944 the control of estuarine stratification, *Estuaries*, 13, 125-132, 10.2307/1351581, 1990.

945 Van Maren, D. S., van Kessel, T., Cronin, K. and Sittoni, L.: The impact of channel deepening and
946 dredging on estuarine sediment concentration, *Cont. Shelf Res.*, 95, 1-14, 2015.

947 Wang, T., Geyer, W. R., Engel, P., Jiang, W. S. and Feng, S. Z.: Mechanisms of Tidal Oscillatory Salt
948 Transport in a Partially Stratified Estuary, *J. Phys. Oceanogr.*, 45, 2773-2789, 2015.

949 Waterhouse, A., Tutak, B., Valle-Levinson, A. and Sheng, Y.: Influence of Two Tropical Storms on the
950 Residual Flow in a Subtropical Tidal Inlet, *Estuar. Coast.*, 36, 1037-1053, 10.1007/s12237-013-
951 9606-3, 2013.

952 Willmott, C. J.: On the validation of models, *Phys. Geogr.*, 2, 184-194, 1981.

953 Wilson, R. and Filadelfo, R. 1986. Subtidal Current Variability in the Lower Hudson Estuary. Springer -
954 Verlag, Berlin, Germany. p. 132-142.

955 Winterwerp, J. C.: Fine sediment transport by tidal asymmetry in the high-concentrated Ems River:
956 indications for a regime shift in response to channel deepening, *Ocean Dynam.*, 61, 203-215, 2011.

957 Zhang, R., Chen, L. H., Liu, S. S., Zhang, H. and Lin, G. Y.: Shoreline evolution in an embayed beach
958 adjacent to tidal inlet: The impact of anthropogenic activities, *Geomorphology*, 346, 106856, 2019.

959 Zhu, J., Weisberg, R. H., Zheng, L. Y. and Han, S. Z.: Influences of Channel Deepening and Widening
960 on the Tidal and Nontidal Circulations of Tampa Bay, *Estuaries & Coasts*, 38, 132-150, 2015.

961 Zhu, L. 2018. Alteration of estuarine circulation under the inference of morphological evolution. East
962 China Normal University, Shanghai, China.

963